# Investigating the Black Hole in M87

Michael Drew

A thesis submitted in partial fulfilment
of the requirements for the degree of
Master of Science

Jeremiah Horrocks Institute for Mathematics, Physics and Astronomy
University of Central Lancashire

February 2025

# Declaration

**Type of Award:** Master of Science

**School:** Physical Sciences and Computing

I declare that while registered as a candidate for the research degree, I have not been a registered candidate or enrolled student for another award of the University or other academic or professional institution.

I declare that no material contained in the thesis has been used in any other submission for an academic award and writing of the thesis was entirely my own work. Although I carried out all the measurements and calculations, I received assistance with the following: i) In Chapter 3, Dr. Patterson prepared Figure 3.10, which overlays brightness contours from 2018 M87* observations on the 2017 image; ii) In Chapter 5, Dr. Walton improved the mathematical rigour of the thin/disk modelling and prepared Figure 5.2.

No proof-reading service was used in the compilation of this thesis.

Michael Drew

February 2025

# Abstract

This study investigates the supermassive black hole in M87, a key target of the Event Horizon Telescope (EHT) Collaboration, that has proved a fruitful laboratory for astrophysics research. Progress in developing the capabilities of the EHT, by exploiting VLBI and enhancing data processing, imaging and analysis techniques, has delivered breakthroughs in imaging and polarisation results. While the mass of M87* is well constrained, obtaining a consensus on its spin has proved challenging, evidenced by the wide range of published results. The author sets out new methods to estimate the spin and accretion rate of the black hole, based on some key assumptions. Using EHT Collaboration imaging results of M87*, the rotational velocity of the inner edge of the accretion disk is estimated as $\sim (4.2 \pm 0.3) \times 10^7$ m $s^{-1}$, or $\sim 0.14$ c, leading to a spin parameter of $a \sim 0.8 \pm 0.1$. Investigation of EHT Collaboration polarisation results, the location of the innermost stable circular orbit, plasma density and the accretion model yields further parameters. The accretion velocity is estimated at $\sim (7 \pm 0.7) \times 10^7$ $ms^{-1}$ and the accretion rate from the inner disk spans a range from $\sim (4 \times 10^{-5}$ to $4 \times 10^{-1})$ $M_{\odot}yr^{-1}$. The accretion power is estimated in the range $\sim 10^{34}$ to $\sim 10^{38}$ $Js^{-1}$, which aligns with accretion-driven jet models.

# Contents

# Acknowledgements

I would like to express sincere appreciation to my supervisors, Professor Derek Ward-Thompson and Dr. Brett Patterson. They have always been encouraging and supportive and I have benefitted greatly from their expertise. I also thank Dr. Timothy Walton, who participated in our supervision meetings.

# Abbreviations

| | |
|---|---|
| EHT | Event Horizon Telescope |
| EHTC | Event Horizon Telescope Collaboration |
| SMBH | Supermassive Black Hole |
| VLBI | Very Long Baseline Interferometry |
| GR | General Relativity |
| GRMHD | General-relativistic magnetohydrodynamic simulation |
| Mass of Sun | $M_\odot$ |
| Parsec | $3.09 \times 10^{16}$ m |
| ISCO | Innermost stable circular orbit |

# Chapter 1

# Introduction

## 1.1 Introduction

This study investigates the supermassive black hole (SMBH) at the centre of M87. The black hole, referred to hereafter as M87*, is approximately six and a half billion times the mass of the Sun. Its host is an elliptical, low redshift ($z \sim 0.004$) radio galaxy, located at a distance of $\sim$ 17 Mpc in the Virgo cluster of galaxies (Matveyenko & Seleznev, 2011). This work focuses on recent progress made in M87* research and aims to contribute, in particular, to the discussion on its spin and accretion rate.

The investigation of SMBHs is an important research topic in astrophysics, given observational evidence that they exist at the centre of nearly all local large galaxies (Berti & Volonteri, 2008) and play a significant role in the formation and evolution of their host galaxies − e.g.: Richstone et al. (1998); Reynolds (2019a). For example, SMBHs can launch powerful jets, which distribute energy back from the core into the interstellar medium and impact on the evolutionary pathway of galaxies by affecting star formation (Heckman & Best, 2014). Their astrophysical importance has stimulated a period of significant research activity, described as a 'golden age' for black hole physics and, in particular, the investigation of black hole spin (Reynolds,

2019b).

A notable initiative has been the Event Horizon Telescope Collaboration (EHTC), whose principle goal is to image SMBHs on event horizon scales. This international partnership has developed a virtual telescope, with sufficient angular resolving power from the Earth's surface to produce an image of a black hole. M87* was chosen as a key observational target of the EHTC. The first image of the black hole was published in April 2019 (see Figure 1.1), representing a significant milestone in astrophysics research. The EHTC has made transformational progress by exploiting improvements in very-long-baseline interferometry (VLBI), in order to achieve an angular resolution comparable to the event horizon of M87*, which made the first image possible (EHTC et al., 2019a). Since the 2017 observational programme, the EHTC has published its findings in eight detailed papers related to M87*, which have provided a core resource for this study.

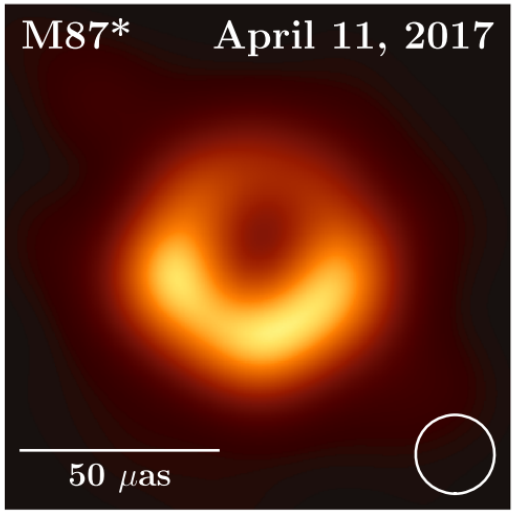


Figure 1.1: *First M87* image from EHT observations in April 2017. Image credit: EHTC et al. (2019b), Figure 3.*

The work of the EHTC, in which UCLAN has been closely involved, stimulated the author's interest in researching this topic. The focus of the study is on investigating the key parameters of M87*, using a relatively simple mathematical approach

and basic principles of physics. In particular, the study examines the angular momentum of M87*, given the lack of consensus on the level of spin in published studies, which is discussed in this work. It seeks to contribute to the discussion on this challenging aspect, by discussing a new method to estimate spin, as well as estimating the accretion rate onto M87* and considering other key parameters.

## 1.2 Background

While the term 'black hole' was invented by Wheeler in 1967, they were predicted independently in the eighteenth century by the pioneering work of Michell and Laplace. In 1915, Einstein developed his theory of general relativity (Einstein, 1915). According to GR, black holes have a profound effect on their immediate environment, as their immense mass curves spacetime in their vicinity - e.g. Wald (2010). A black hole is a region of spacetime where gravitational forces are so strong that the escape velocity exceeds the speed of light. As a result, events inside this event horizon cannot be seen by any external observer. The largest category of black holes by mass are SMBHs, such as M87*, which are thought to exist at the centre of most large galaxies (Frolov & Zelnikov, 2011).

During the last 50 years, there has been much theoretical research and discussion on the properties of black holes and how they interact with their environment - e.g. Bardeen et al. (1972). Increasing focus on the study of the most massive category of SMBHs has been stimulated by a growing awareness of their importance in the development of galaxies. The main drivers of their mass and spin, since formation billions of years ago, are likely to have been mergers with other black holes and ongoing accretion of gas from the central region of the galaxy (Volonteri et al., 2005). As SMBHs evolve, they can also produce powerful outflows, such as the M87* jet, which feed matter and energy back into the nearby environment, thereby influencing

galaxy development through, for example, star formation - e.g. Fabian (2012).

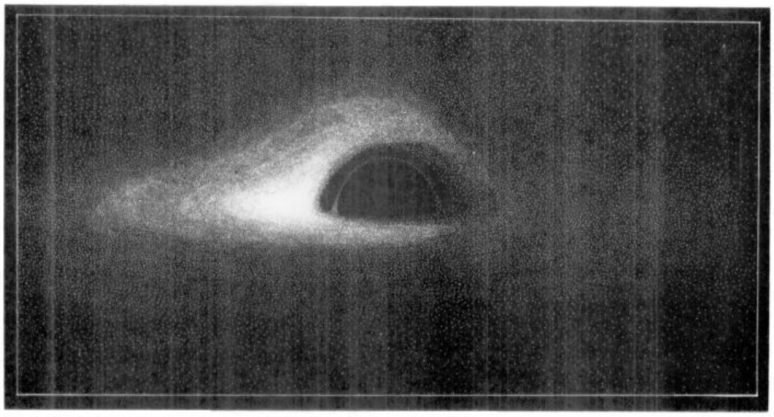

Figure 1.2: *A simulated photo of a black hole, assuming a thin accretion disk, which was published in 1979. Image Source: Luminet (1979), Figure 1.*

Several decades ago, it was predicted that black holes could be observed and Luminet (1979) constructed a photograph simulating the optical appearance of a black hole. This image (Figure 1.2), which includes a bright emission ring enclosing a dark shadow, now seems remarkably accurate, taking into account that research on black holes was, at that stage, largely theoretical. Luminet predicted a black circle (it was not yet described as a shadow), within a bright accretion disc, having one side clearly more luminous than the other (as a result of the Doppler effect). While theoretical predictions have become more refined and detailed over time, the observational capability to resolve the event horizon scale of a black hole represents a step change in research progress. Continued efforts to improve techniques and enhance data quality have maintained this momentum.

Although black holes may seem rather enigmatic, our current understanding is that they have only three defining properties, mass, angular momentum and electric charge (Gürlebeck, 2015). Mass estimates for many black holes have been published, including M87* (EHTC et al., 2019f). However, while angular momentum is also a fundamental characteristic of black holes, it has proved difficult to constrain the spin

parameter (Brenneman, 2013). Resolving this problem has been described as one of the grand challenges of astrophysics (Kawashima et al., 2019). While electric charge is, in principle, also one of a black hole's three fundamental properties, it is argued that it would be neutralised in most environments, as the black hole would accrete roughly equal numbers of particles with opposite charges (Brenneman, 2013).

As an understanding of SMBH spin can contribute to a deeper knowledge of astrophysical processes at the core of galaxies, investigating angular momentum has become an important and active area of research. The development of new techniques to measure spin, including studies probing the nature of spacetime in the strong gravitational field, close to the event horizon, have provided useful insights into the physical processes at the core of black holes (Brenneman, 2013). For example, some studies have investigated how the jet power of a black hole relates to its spin e.g. Tchekhovskoy et al. (2011a), which has improved understanding of complex accretion and outflow processes close to the core. However, whilst much progress has been made, inferring black hole spin remains a challenge, due largely to current limitations in observational capabilities.

## 1.3 The Event Horizon Telescope Collaboration

The EHTC is an international alliance, that was formed to develop VLBI at short wavelengths, in order to study the emission region of SMBHs. The EHT instrument comprises a group of radio telescopes located at selected sites around the world, which operate together as a virtual instrument. Following numerous successful initiatives to improve performance, it has recently achieved a resolution sufficient for detailed study of M87* and SgrA*, the black hole at the centre of our own galaxy. These black holes were chosen as the primary targets of the EHTC because they

present to Earth the largest angular sizes of known SMBHs, which makes them attractive targets for observation (EHTC et al., 2022a).

The success of the EHTC in imaging M87* has been transformational in advancing our understanding of black holes. This progress has been closely linked with major enhancements to radio telescope instrumentation and techniques, together with related data processing and computational image reconstruction. It has enabled predictions from theoretical work to be compared with observational results, to probe our understanding of key black hole processes. In particular, recent observational data has been compared with the results of general relativistic magnetohydrodynamic (GRMHD) simulations, which model magnetized plasma evolving in a Kerr space-time (see example in Figure 1.3.) The availability of new observa-

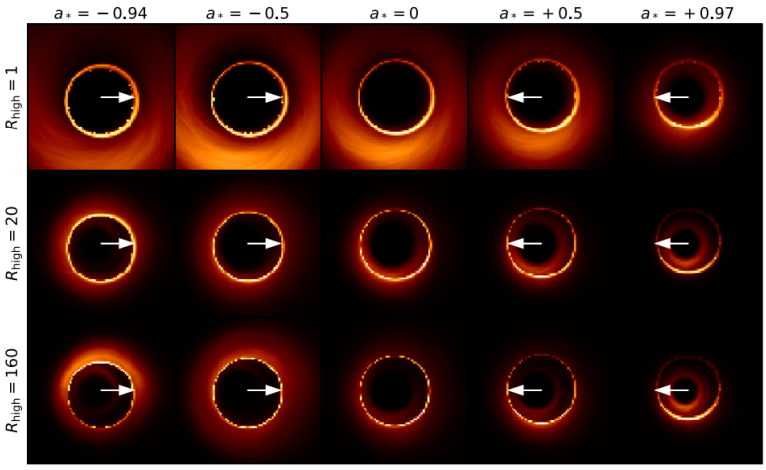


Figure 1.3: *An example of M87* images generated by GRMHD simulations with a range of spins. Image credit: EHTC et al. (2019e) Figure 2.*

tional data has stimulated further research efforts, enabling theories to be tested and the results of simulations to be compared with actual data. However, it has also highlighted the limitations of current data and confirmed the need for further enhancements to observational capabilities.

M87* has a mass 1,500 times larger than SgrA*, but is located 2,000 times more

distant from Earth. Some parameters, such as ring diameter, appear to scale linearly with its mass, as the radius of the event horizon in M87* is approximately a thousand times larger than that of Sgr A*. Clearly the physics determining the ring size is driven predominantly by the masses of these black holes. In contrast, whilst it might be expected that the luminosity will also scale with mass, M87* is $\approx 10^6$ more luminous than Sgr A*. Perhaps luminosity scales with the square of the mass. However, accretion onto M87* is estimated as $\approx 10^6$ times higher than Sgr A*. This would suggest that the the luminosity scales proportionally to the accretion rate, rather than the mass of the black hole. Thus, an elementary overview of key parameters suggests that astrophysical processes have influenced the development of M87* and Sgr A* in very different ways.

In 2017, the EHTC undertook an observational programme to gather detailed data on these two primary targets. It was subsequently decided to prioritise the production of an image of M87*, as it was found to be a more stable source. While EHT images of M87* from observations on consecutive nights are very similar (EHTC et al., 2019d), the source structure of Sgr A* was found to change within a much shorter timeframe. In 2021, the success in imaging M87* was followed by the publication of polarised images. These allow researchers to probe the strength and orientation of magnetic fields at the core of M87*, which are thought to play a significant role in important processes, such as jet launching. In 2024, a second image of M87* was published by the EHTC from 2018 data (Figure 1.4), revealing a remarkably similar ring morphology as the first image (EHTC et al., 2024). Confirmation of a comparable structure using a completely new data set is of considerable scientific importance, as it demonstrates the reproducibility of the original results.

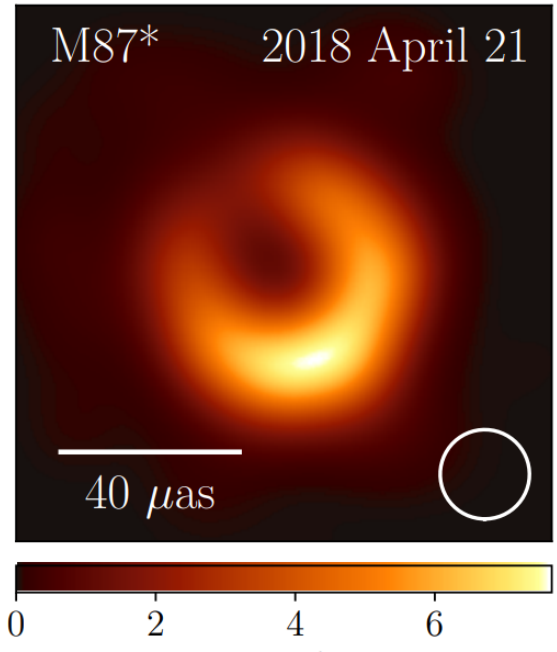


Figure 1.4: *M87* image from EHT observations in April 2018, one year after data for the first image was obtained. Image credit: EHTC et al. (2024), Figure 1 (right hand side).*

## 1.4 Structure of thesis

The thesis is structured as follows. Chapter 2 provides background in relation to the physics of black holes, including a description of their fundamental characteristics and main parameters, including mass, spin, accretion rate and jet power. Following an estimate of M87* mass, the focus is on different techniques used to assess its angular momentum and the results obtained from a range of studies. Chapter 3 investigates the EHT instrument, which is based on the principles of VLBI. It assesses progress in observations, data processing and data analysis techniques that made possible the first images of M87*. Important research outputs that are used in this study, including images and polarisation maps, are also reviewed. Chapter 4 sets out a proposed new method to assess the angular momentum and spin parameter

of M87*. It explains the key assumptions made and discusses the results in a comparative context. Chapter 5 extends the analysis undertaken in Chapter 4, leading to estimates of other key M87 parameters. These include the accretion rate onto the black hole and the accretion power. The underlying assumptions behind these estimates are explained. Chapter 6 summarises the main findings and conclusions. It draws on the analysis of previous chapters to set out the limitations of the study and identifies future work required to progress M87* research. It includes a brief review of current projects planned, or in progress, to address these challenges, which are of significant astrophysical importance.

# Chapter 2

# The Black Hole in M87

## 2.1 Introduction

This chapter investigates the black hole in M87. It considers the physics of a spinning black hole, against a theoretical background underpinned by the fundamental predictions of general relativity (Einstein, 1915). The Kerr solution to the Einstein field equations provides a basis to measure the mass and spin of a black hole. The key elements of the M87* black hole system are described, including the accretion disk and relativistic jet. The mass of M87*, the first fundamental parameter of the Kerr metric, is estimated using a simplified approach. Finally, the main approaches to constraining the spin of M87* are reviewed, together with the varied results obtained from a range of studies.

## 2.2 The physics of M87*

### 2.2.1 Fundamental characteristics

Einstein's theory of general relativity (GR) predicted the existence of black holes, a region of spacetime where the gravitational field is sufficiently great that no

information-carrying objects and signals can escape (Einstein, 1915). The solution to Einstein's field equations indicates that a black hole is formed when a gravitating object becomes less than its gravitational radius. For a non-spinning object of mass, $M_{BH}$, this is also known as the Schwarzschild radius, $R_s$. The boundary at this radius acts as the event horizon in a non-rotating body, referred to as a "radius of no return" (Meier, 2012) and is determined by the equation (Foster & Nightingale, 2006, p.152):

$$R_s = 2GM_{BH}/c^2 \tag{2.1}$$

The size of a black hole, in terms of the radius of its event horizon, is thus proportional to its mass, which suggests a method to estimate the latter.

An astrophysical black hole is expected to rotate, but angular momentum cannot be directly measured and thus has to be inferred (Foster & Nightingale, 2006, p.159). The spin of a black hole is measured using a dimensionless variable, a, which has a range from $-1$ to $+1$ (Reynolds, 2021b). Prograde rotation (a>0) indicates that the spin is in the same direction as the disk, while retrograde rotation (a<0) denotes that the black hole and disk spin in opposite directions. If a black hole were to form without angular momentum, it is argued that it would obtain spin from interaction with the surrounding matter (Frolov & Zelnikov, 2011). Matter drawn towards the outer regions of the black hole system is transported slowly to the inner region of the accretion disk, eventually reaching the innermost stable circular orbit ($R_{ISCO}$). This orbit is an important parameter in studying black holes, being the radius of the last predominantly stable orbit for a particle about to fall through the event horizon. It is expected that matter falling into the black hole from this orbit carries angular momentum, which increases the rotation of the black hole (Lynden-Bell, 1969).

If a black hole has non-zero spin, GR shows that the event horizon radius, R,

is smaller than for a non-spinning object (Reynolds, 2013). As the rate of spin increases, R decreases until, at a maximum spin parameter of a=1,

$$R = GM_{BH}/c^2 \tag{2.2}$$

Before discussing how spin is measured, it is necessary to consider what is meant by the rotation of a black hole. In the early 1960s, Kerr found an exact solution to the Einstein field equations (Kerr, 1963), which provide a mathematical description of a rotating black hole without electric charge (Foster & Nightingale, 2006).

In 'Boyer-Lindquist' coordinates, with spacetime coordinates (t, r, $\theta$, $\phi$), where t is time, $\theta$ and $\phi$ are polar angles and r is a radial coordinate, the Kerr metric has the form

$$c^2 d\tau^2 =$$

$$(1-\tfrac{2mr}{\rho^2})\, c^2 dt^2 + \tfrac{4mcra\, sin^2\theta}{\rho^2} dt d\phi - \tfrac{\rho^2}{\delta} dr^2 - \rho^2 d\theta^2 - ((r^2+a^2) sin^2\theta + \tfrac{2mra^2\, sin^4\theta}{\rho^2}) d\phi^2, \tag{2.3}$$

where m is the mass of the black hole, a is its angular momentum per unit mass (0 $\leq$ a $\leq$ m), and the functions $\delta$ and $\rho^2$ are

$$\delta = r^2 + a^2 - 2mr, \tag{2.4}$$

$$\rho^2 = r^2 + a^2 \cos^2\theta. \tag{2.5}$$

The Kerr solution leads to an understanding that, as a black hole rotates, it drags spacetime around with it. This 'twisting' of spacetime in the vicinity of a spinning black hole is aptly named frame-dragging, as the local frame of reference is dragged around it (Foster & Nightingale, 2006, p.161). This effect becomes extreme in close proximity to the black hole and within the ergosphere, which is the region inside the static limit ($r < GM_{BH}/c^2$), where both matter and light are compelled to rotate in the same direction as the black hole (Reynolds, 2021a).

If we consider that a black hole has mass, $M_{BH}$, and angular momentum, J,

the 'unitless' spin parameter, a, is defined (Reynolds, 2019b) by

$$a = cJ/GM_{BH}^2, \tag{2.6}$$

where c is the speed of light and G is Newton's gravitational constant. An estimate of J and $M_{BH}$ thus enables the spin parameter to be constrained.

### 2.2.2 Anatomy of M87*

M87* is described as a supermassive black hole, as it is within the largest mass range of $\sim 10^6$ to $10^9 M_\odot$ (Brenneman, 2013). The key elements of the M87* system are briefly summarised below.

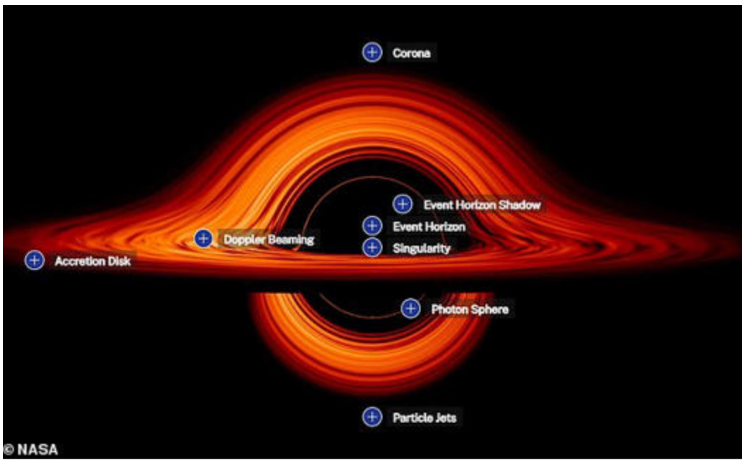


Figure 2.1: *A visualisation of a black hole seen nearly edgewise, with key features indicated. It is surrounded by a turbulent disk of plasma. Image Credit: NASA's Goddard Space Flight Center/Jeremy Schnittman. Available at: www.nasa.gov/universe/nasa-visualization-shows-a-black-holes-warped-world/*

#### Event Horizon

The event horizon is the defining feature of a black hole, the outer boundary from within which a particle cannot escape. Inside the event horizon, the velocity needed

to escape the black hole exceeds the speed of light (Foster & Nightingale, 2006, p.163). This means that photons, for example, which originate on or inside the event horizon, cannot reach an observer outside its radius.

### Event Horizon Shadow

The event horizon captures any light passing through it, and the distortion of space-time in the intense gravitational field around the black hole causes the bending of light, through gravitational lensing. These two effects produce a dark zone or 'shadow', that is essentially an image of the event horizon.

### Photon Sphere

The photon sphere is located farther from the centre of a black hole than the event horizon. Thin rings of light are distorted images of the disk. Photons here may orbit the black hole many times before escaping. Nearer the core, these photon rings become fainter and thinner.

### Accretion Disk

As illustrated in Fig. 2.1, the accretion disk, which is an intrinsic part of the black hole system, is a hot, bright, spinning disk, composed of gas that orbits the black hole. The disk is fed from the central region of the host galaxy, as matter is drawn towards the core by the black hole's gravitational field. As matter approaches the event horizon, it loses gravitational energy and becomes hotter, as a result of friction. This process is not fully understood, but it may be a type of viscosity, enabled by the prevailing magnetic fields (Shakura & Sunyaev, 1973), which causes the disk to dissipate energy (King et al., 2007). The process is fundamental to transporting angular momentum away from the core and enabling gas to spiral inwards. The accretion rate onto the black hole is an important parameter, which indicates its

growth in mass over time. It is normally measured in solar masses per year.

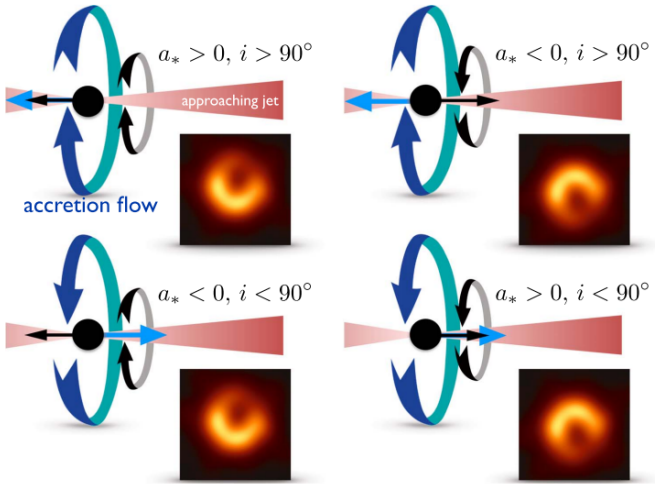


Figure 2.2: *Illustration of ring asymmetry from Doppler beaming effect arising from disk and black hole angular momentum. The larger arrow (blue) indicates the direction of disk rotation, while the smaller arrow (black) shows the spin. The inclination, i, is the angle between the disk angular momentum vector and the line of sight. Image credit: EHTC et al. (2019e), Figure 5.*

As illustrated in Figure 2.2, the first M87* image revealed a north-south asymmetry in the accretion ring, assumed to arise from the Doppler beaming effect, as matter on one side of the disk approaches Earth, while the other side recedes (EHTC et al., 2019e). Alignment of the black hole spin axis with the jet facing the right (see Figure 2.2) indicates that the black hole is rotating clockwise, as observed from Earth.

### Innermost Stable Circular Orbit (ISCO)

While gas encircling the black hole remains at some distance from the core, Newton's law of gravity prevails and the gas is transported in predominantly stable circular motion, slowly drifting inwards. However, relativistic effects become pronounced

as the gas approaches close to the black hole and the circular orbits become destabilised. General relativity predicts that the ISCO, as the name implies, is the last stable circular orbit for a particle revolving around the black hole (Reynolds, 2019b). Once material orbiting within the accretion flow loses angular momentum and moves closer to the black hole than $R_{ISCO}$, it is expected to plunge beyond the event horizon into the black hole. This is supported by GRMHD simulations of accretion disks, indicating that at ISCO there is a rapid transition to a plunging flow (Reynolds & Fabian, 2008).

**Jet**

A distinctive feature of the M87* system is the powerful, relativistic jet, which streams from its centre, extending 1.5 kpc from the core (see Figure 2.3). The highly collimated, gaseous jet source has an age estimated at about 40 Myr (de Gasperin et al. 2012). As in many other active galactic nuclei, the jet redistributes matter throughout M87, thereby influencing the evolution of the galaxy (Richstone et al., 1998). There is ongoing research into several aspects of the jet, including the launching mechanism, together with the acceleration and propagation of the ejected plasma as it emerges from the central core region. There is evidence that the edge-brightened jet connects to the accretion flow of the black hole (Lu et al., 2023).

The power of the M87* jet is an important parameter that has been investigated by several studies (EHTC et al., 2019e, and references therein). It is believed that relativistic jets are driven by accreting black holes - e.g. Rees et al. (1982) and Begelman et al. (1984), as these are efficient engines which can explain the observed energetics of such jets. However, the extent to which black hole spin or accretion disk rotation drives these jets is less clear (Meier, 2012). While several theoretical explanations have been put forward to describe the processes involved, the extent that jet formation is driven by the spin of the black hole is currently uncertain

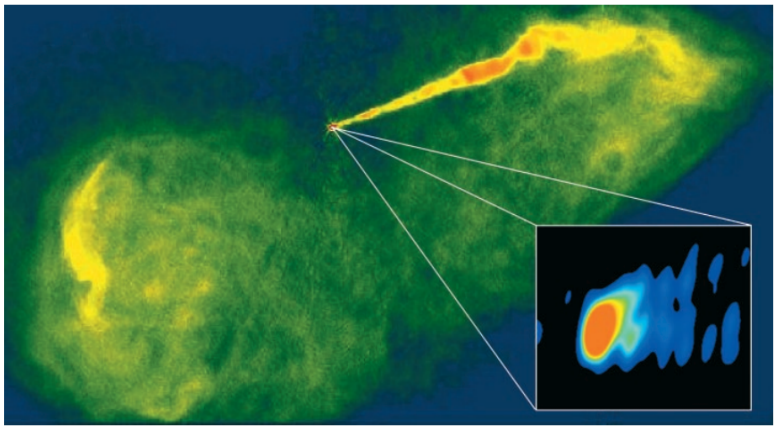

Figure 2.3: *The image shows the approaching (northwest) M87* jet, which is Doppler boosted. The other south east jet, which radiates away from Earth, is difficult to detect. The lobes contain decelerated jet material and radiate isotropically. The inset shows an initial wide opening angle (60°) from the core region, which reduces as the jet emerges. The length of the jet emission in the inset is* $\sim 0.001$ *arc sec, which is only* $\sim 250$ *times the Schwarzschild radius of the black hole. Image Credit: (Meier et al., 2001a, Figure 1)*

(McKinney, 2006). A further unresolved aspect is how jet formation is influenced by a prograde or retrograde spin (Garofalo et al., 2010). The characteristics of the M87 jet are similar to many other relativistic jets (Meier et al., 2001a).

There is no consensus on the jet launching mechanism, although it is likely to be powered by the accretion disk (Meier et al., 2001). Studies of the jet launching region suggest it is located at the core of M87*, with a core size of $\sim 5.5 \pm 0.4 R_s$, where $R_s$ is the Schwarzschild radius (Doeleman et al., 2012). Observations indicate that there is a stratification of jet emission velocities (Park et al., 2019), with various streamlines at ejection speeds of $\sim 0.9c$ (Meier et al., 2020).

## 2.3 Estimating M87* mass

As in the case of spin, the mass of M87* can only be inferred. While the masses of relatively small (stellar-mass) black holes may be measured by analysing the orbital and radiative properties of nearby stars, estimating the mass of SMBHs, such as M87*, is more challenging (Foster & Nightingale, 2006). An early study, using photometry data from the Palomar 60-in. and 200-in. telescopes, predicts a supermassive object of $\sim$ 5 billion solar masses (Young et al., 1978). Two more recent estimates are noteworthy, as they used high-quality data and advanced modelling (EHTC et al., 2019f). Gebhardt et al. (2011) observed the central $2''$ ($\sim 150pc$) region of M87 with the Gemini telescope integral-field spectrograph (NIFS). Using data from infrared spectroscopic observations of stellar absorption lines, they studied the stellar velocity distributions and measured an increase in the tangential velocity anisotropy of stars orbiting in the core region with decreasing radius. The study concluded that the observed stellar kinematics cannot be explained without assuming a central compact object with an estimated mass of $M_{BH} = (6.6 \pm 0.4)$ $\times 10^9 \mathrm{M}_\odot$.

A different approach by Walsh et al. (2013), based on gas-dynamical fitting rather than stellar dynamics, reported a significantly lower figure of $M_{BH} = 3.5 \times 10^9 \mathrm{M}_\odot$. Their research was based on Hubble Space Telescope (HST) Space Telescope Imaging Spectrograph observations of $H\alpha$ and $NII$ emission lines from the gas-disk close to the M87 nucleus. The data enabled mapping of the velocity field within 40pc of the black hole. Progress has recently been made to understand the differences in results between these two different approaches. For example, Jeter et al. (2019) point out that gas-dynamical modelling assumes that the circulating gas flows on Keplerian orbits, which they argue is a weakness in this method. They present a non-Keplerian velocity model, which is able to reconcile the discrepancy between mass estimates based on gas dynamics and stellar kinematics. Their estimate of

$M_{BH} = 6.5 \times 10^9 \mathrm{M}_\odot$ aligns with EHTC et al. (2019a).

In 2017, the EHT achieved the high resolution required to resolve horizon scales for M87. This enhanced observational capability led to an unprecedented constraint on the mass of the black hole (Nemmen, 2019a). From analysing this new data, the EHTC was able to establish the physical length scale of the emission region from its angular size (EHTC et al., 2019f). It reported a systematic uncertainty in determining the location of the mean emission diameter in GRMHD simulations, used when converting from an angular to a physical estimate. In addition to this source of systematic uncertainty, estimated at $\sigma_{sys} = 0.7 \times 10^9 \mathrm{M}_\odot$, the EHTC noted a lower level of uncertainty in the angular diameter estimate of $\sigma_{stat} = 0.2 \times 10^9 \mathrm{M}_\odot$. Reflecting these limitations, the mass of M87* is estimated as $M = 6.5 \pm 0.2$(stat) $\pm 0.7$(sys) $\times 10^9 \mathrm{M}_\odot$ (EHTC et al., 2019f). This result is in agreement with the earlier mass measurement, based on stellar dynamics (Gebhardt et al., 2011).

EHTC's method of deriving the mass of M87* is based on its estimate of the black hole gravitational radius, $\theta_g$. The angular size of the gravitational radius is defined by EHTC et al. (2019a) as:

$$\theta_g = \frac{G\, M_{BH}}{D\, c^2}, \tag{2.7}$$

where D is the distance to M87*. The gravitational radius, which sets the physical length scale of the emission region, was estimated by obtaining the best fit from comparing geometric crescent models to the observational data. The models that most closely match the data for the asymmetric emission ring have diameters of 42 $\pm$ 0.9 $\mu$as (EHTC et al., 2019a). The gravitational radius, $\theta_g$, was estimated from $d/\alpha$, where d is the measured diameter of the observable ring, while $\alpha$ is a scaling factor estimated from EHTC models at $\sim$10.7 to 11.5. This led to an estimate for $\theta_g$ of $3.8 \pm 0.4 \mu as$ (EHTC et al., 2019f).

We can use this result to obtain an estimate for $M_{BH}$. Rearranging equation 2.7

gives:

$$M_{BH} = \frac{D\, c^2\, \theta_g}{G} \tag{2.8}$$

$M_{BH}$ may be calculated, using the estimated value of the gravitational radius (converted to radians) and the established measurement of the distance to the black hole, D = 16.8Mpc, as follows:

$$M_{BH} = \frac{D\, c^2\, \theta_g}{G} = \frac{(5.18 \times 10^{23}) \times (3 \times 10^8)^2 \times (1.84 \times 10^{-11})}{6.67 \times 10^{-11}} \tag{2.9}$$

Thus $M_{BH} = 12.86 \times 10^{39}$ kgs, or $6.4 \times 10^9 M_\odot$. This simplified calculation aligns with the published EHTC estimate discussed above.

## 2.4 Approaches to measuring M87* spin

Several different techniques have been used to estimate the spin of M87*. In general, each approach seeks to measure a black hole parameter that has been shown, theoretically, to have a relationship with the spin parameter. For example, for a Kerr black hole, $R_{ISCO}$, the radius of ISCO, is an astrophysically important location, as it is theoretically linked to the spin parameter. Apart from determining $R_{ISCO}$, examples of other approaches used to estimate spin include measuring the black hole shadow and modelling the black hole as an engine, which involves analysing the energetics of the system. These three important, but very different, approaches are briefly outlined, followed by an overview of M87* spin estimates obtained by eight different studies, which produce estimates spanning a wide range of spin parameters.

This review is restricted to methods that have been used to estimate the spin of M87*. Some other widely used techniques to measure black hole spin are not viable options for M87*. For example, x-ray reflection spectroscopy, which involves the analysis of reflection features in the spectra of black holes (Bambi et al., 2021), is a popular method to estimate the spins of accreting black holes (Mall et al., 2024). However, it is not suitable for constraining the spin of M87*, as it does not meet

the important requirements (e.g. broad Fe K$\alpha$ line of sufficient strength) set out by Brenneman (2013).

### 2.4.1 The innermost stable circular orbit (ISCO)

ISCO depends on the spin of the black hole and moves nearer the centre as the level of spin increases. Therefore, locating the position of ISCO is a widely used method to constrain black hole spin. A simplified diagram of the inner accretion disk (Figure 2.4) shows the change in disk structure at ISCO.

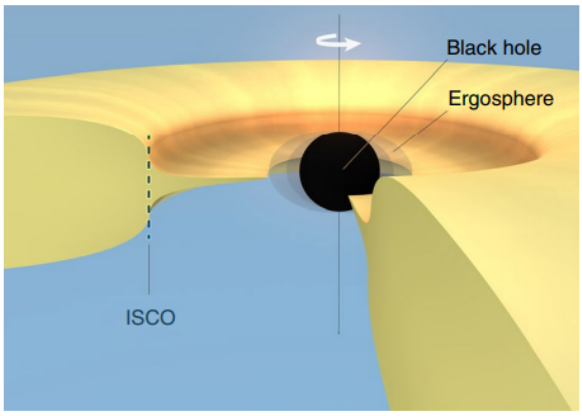


Figure 2.4: *Diagram of inner regions of a thin accretion disk, showing how the structure of the disk changes at ISCO. Image credit: Reynolds (2019b).*

The theoretical relationship between ISCO and the spin parameter is illustrated in Fig. 2.5. The radius at ISCO, $R_{ISCO}$, can be estimated generally (Bardeen et al., 1972), formula 2.21, as follows

$$R_{ISCO} = M(3 + Z_2 \mp (3 - Z_1)(3 + Z_1 + 2Z_2)^{1/2}), \tag{2.10}$$

where

$$Z_1 = 1 + (1 - a^2)^{1/3}[(1 + a)^{1/3} + (1 - a)^{1/3}] \tag{2.11}$$

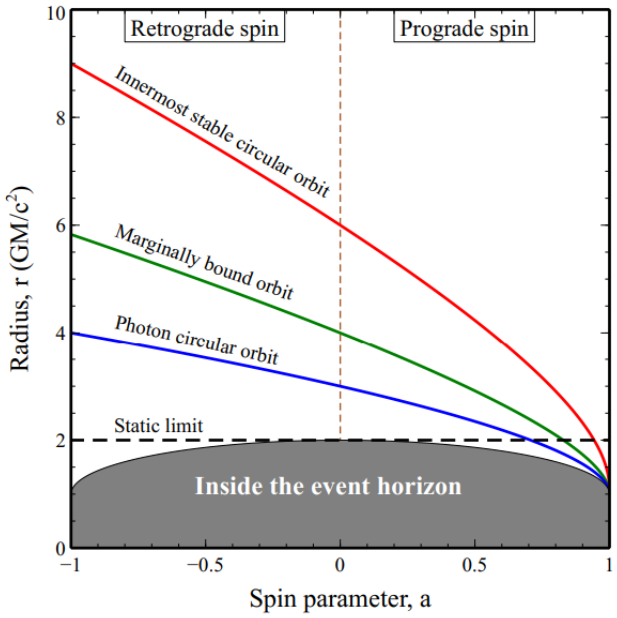


Figure 2.5: *Sketch illustrating the radius of the ISCO and other special orbits (for a Kerr black hole) versus spin parameter, a. Image credit: Reynolds (2021c).*

and

$$Z_2 = (3a^2 + Z_1^2)^{1/2} \tag{2.12}$$

The $-/+$ sign indicates particles in prograde/retrograde motion respectively.

Solutions to the above equations (Reynolds, 2021b) show that ISCO is located at $6GM/c^2$ (equivalent to $3R_s$) for a non-spinning black hole (a=0). However, for a pro-grade spinning black hole, frame-dragging can stabilise otherwise unstable orbits, moving the ISCO closer to the black hole, while retrograde orbiting particles tend to have a destabilising effect and ISCO moves further from the core. As a result, the ISCO for a maximally spinning black hole (a=1 or $-1$) varies from $1GM/c^2$ for a prograde orbit to $9GM/c^2$ for retrograde motion.

Although particles on circular orbits in the symmetry plane of the black hole spin experience frame dragging, if the trajectory of the orbiting particle is not aligned

with the spin (ie not in the $\theta = \pi/2$ plane), the orbital plane will be subject to precession (Sob'yanin, 2018).

### 2.4.2 The black hole shadow

For the first time, data obtained from EHT's 2017 observations of M87* enabled imaging of the dark shadow caused by gravitational light bending and photon capture at the event horizon (EHTC et al., 2019a). This success opened up the possibility of estimating the spin of the black hole, by measuring the size and shape of the shadow it casts on the surrounding emission. In the case of a spinning black hole, a frame-dragging effect causes the shape of the shadow to be deformed (Frolov & Zelnikov, 2011).

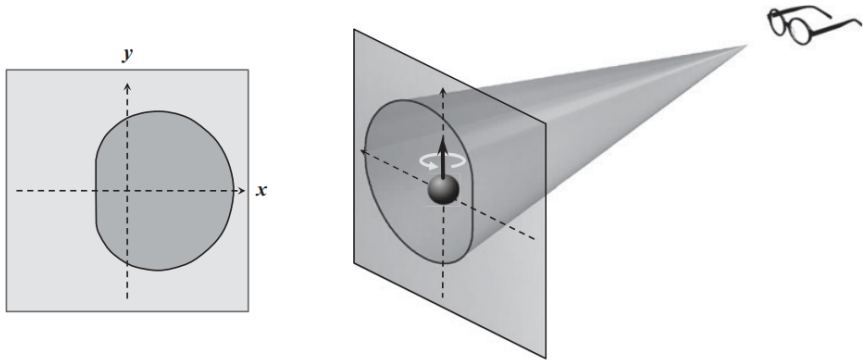


Figure 2.6: *In the case of a spinning black hole, GR predicts that the observer (right hand side) views the black hole shadow as a non-axisymmetric disk, that is displaced slightly to the right (the direction of rotation). Image credit: Frolov & Zelnikov (2011).*

The results of theoretical modelling (see Figure 2.7) show that, for equatorial observers ($i = 90°$), the shadow is nearly circular for most spin levels, becoming distorted only when the spin parameter, a, approaches 1. It has been shown, theoretically, that the shadow size is determined by the radius of the photon orbit in its

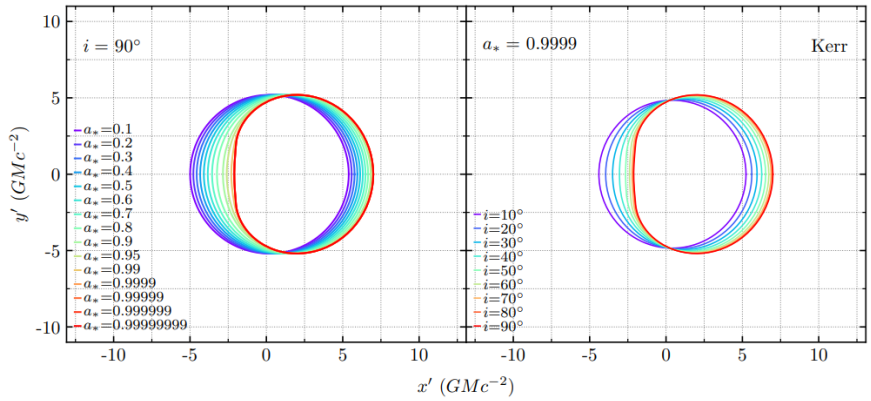


Figure 2.7: *Black hole shadows resulting from the Kerr metric for different values of black hole spin parameter, a (left), and the inclination of the observer, i (right). Image credit: Medeiros et al. (2020).*

spacetime (Bardeen et al., 1972). The radius of this orbit changes significantly with spin, from $3GM_{BH}/c^2$ for a non-spinning black hole to $GM_{BH}/c^2$ for a maximally spinning one in Boyer-Lindquist coordinates and a prograde photon orbit. However, because of gravitational lensing, the size and shape of the black-hole shadow observed at infinity has a very weak dependence on the black-hole spin or the orientation of the observer. For example, the radius reduces by only $\sim 7\%$ (independent of orientation) for a maximally spinning black hole, compared to a non-spinning object (Frolov & Zelnikov, 2011).

Imaging a black hole is potentially an effective method to estimate angular momentum, given theoretical calculations that indicate how the level of spin should affect both the size and shape of the shadow. In practice, because the expected deformation of the shadow is relatively small, particularly for low spin, the angular resolution currently achievable is not yet sufficiently high to discern variations with sufficient accuracy.

Although the current interferometric capabilities of the EHT do not permit precise measurement of the shadow morphology (EHTC et al., 2019c), a null hypothesis

test of the Kerr metric may be made by measuring the size of the shadow (Psaltis et al., 2015). The shadow radius for a Kerr black hole may be estimated from 5±0.2 $GM_{BH}/Dc^2$ for all spins and observer inclinations, assuming $M_{BH}$ and the distance from Earth, D, are known (Medeiros et al., 2020). Therefore, a test of GR may be carried out by investigating whether the size of the shadow is within the designated range of 4%.

It is instructive to illustrate the null hypothesis test of GR, using a simplified approach. The available data for M87* includes its mass, $M_{BH} = 6.5 \times 10^9 M_\odot$ and distance, $D = 5.18 \times 10^{23}$m. The half opening angle, $\theta$, is thus

$$\theta = (5 \pm 0.2) \times \frac{GM_{BH}}{Dc^2} \tag{2.13}$$

$$\theta = (5 \pm 0.2) \frac{(6.67 \times 10^{-11}) \times (6.5 \times 10^9) \times (2 \times 10^{30})}{(5.18 \times 10^{23}) \times (3 \times 10^8)^2} \tag{2.14}$$

This gives $\theta$ =9.3 $\times 10^{-11}$ radians. As 1 microarcsecond = $4.8 \times 10^{-12}$ radians, the angular size of the shadow is expected to be twice the half opening angle $\sim$ 39±2 $\mu as$.

If we turn to the observational results from the EHT Collaboration, the emission ring was measured as having a diameter of 42±3 $\mu$as (EHTC et al., 2019a), which is within the range of theoretical estimates. Thus the measured size of the M87* shadow is consistent with the predictions of the Kerr metric, which constitutes a null hypothesis test of GR (Psaltis et al., 2020). This result has also been confirmed by other studies - e.g. Kumar & Ghosh (2020). In contrast with these findings, it is significant that in the case of other (non-Kerr) metrics, the expected size of the shadow would be significantly different - e.g. Bambi & Freese (2009); Johannsen & Psaltis (2010).

### 2.4.3 The engine paradigm

The energetics of black hole systems have been investigated in several studies, - e.g. Nemmen (2019a), with some using the analogy of an internal combustion engine (Meier, 2012). Using the engine paradigm, it is suggested that, during the accretion process, a black hole acquires mass and angular momentum, which may be regarded as two different kinds of 'fuel'. This energy powers the 'engine', which converts the rotational energy of the black hole system into the observed jet outflow. Ultimately, the rotational energy is derived either from the initial formation of the black hole or during its acquisition of gas and other matter from its surroundings.

Despite decades of research, the physical mechanism that drives jet formation is still unknown (Feng & Wu, 2017) and it is not understood how to accurately infer jet powers observationally (Tchekhovskoy et al., 2011a). These are critical issues to address, as estimates of spin and other parameters using the engine paradigm are based on key assumptions regarding the mechanism that powers the jet. In addition, constraints on the minimum power of the jet have been used to underpin the level of M87* spin and eliminate some models that describe the central engine (EHTC et al., 2019e). The main physical models put forward to explain the dependency of the power of the M87* jet are black hole spin, accretion disk rotation, or a combination of these mechanisms (Meier, 2012). The three prevalent models (Nemmen et al., 2007) are summarised below:

1. Blandford-Payne (BP) model (Blandford & Payne, 1982)
This mechanism explains how the accretion disk can power the jet. The BP process, which describes the impact of rotation on magnetic field lines which are enmeshed through the disk, is driven by different magnetic forces, as illustrated in Figure 2.8. Blandford and Payne explain that, under certain conditions involving rotating magnetic field lines, the plasma is launched as a jet by being unbound from the disk

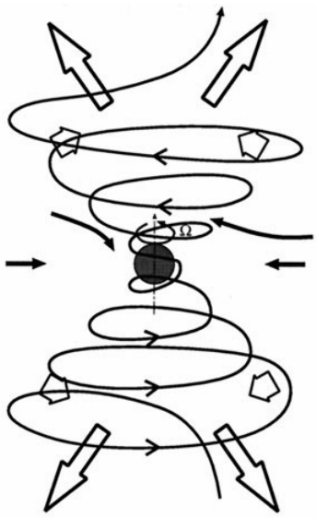

Figure 2.8: *Diagram outlining the BP model, indicating the rotating magnetised plasma moving inward towards the black hole (solid arrows). Magnetocentrifugal forces push the plasma outwards along field lines, while the pressure of the magnetic field has a 'pinching' effect (short open arrows) that lifts plasma and collimates the material (long open arrows) into a jet. Image credit: Meier et al. (2001b), Figure 3.*

and 'flung' outward by centrifugal acceleration. Plasma accumulates in the field lines, generating acceleration from the magnetic pressure gradient, thereby creating a 'spring' motion. The outflowing plasma is then subjected to a magnetic 'pinch', as it is squeezed outwards and collimated in the direction of the rotation axis. This mechanism enables plasma outflows to be launched by the accretion disk itself.

2. Blandford-Znajek (BZ) model (Blandford & Znajek, 1977)

As an alternative to the BP mechanism, the BZ process explains how a magnetised accretion disk can extract black hole rotational energy from a spinning black hole. The magnetic field lines produced by the ionised gas in the accretion disk thread the black hole's spinning ergosphere, twisting the lines from each rotational pole.

The black hole exerts electromagnetic torque on these field lines, thereby transferring rotational energy to jet power. This explains how charged particles within the cylinder of twisted lines are accelerated from the black hole in the form of jets. According to the BZ model, the jet power, $P \propto (a\Phi/M_{BH})^2$, where a is the rotation parameter and $\Phi$ is the magnetic flux threading the event horizon. This model is supported by numerical simulations - e.g. Tchekhovskoy et al. (2011b). In addition, an observational study by Narayan & McClintock (2012) produced evidence that jet power is correlated with black hole spin, mapping closely to the square of the spin parameter, as suggested by the above formula.

It is instructive to consider jets that are produced by other accreting astrophysical objects, such as neutron stars. As these objects do not contain a spinning black hole, the BZ mechanism is not an appropriate explanation for jet production. The jet driving mechanism is sourced from gravitational energy, as matter spirals inwards towards the centre. Material in the rotating disk is able to shed angular momentum, due to viscosity/friction, converting gravitational potential energy to radiation or kinetic energy (such as a jet), that are released from the accretion disk. It is not understood whether the mechanism that drives jets is similar for the range of astrophysical objects that produce them.

3. Hybrid model

A so-called hybrid jet formation model was proposed by Meier (1999). This was subsequently supported by simulation studies, which demonstrate that a combination of black hole spin and accretion power may be important in driving jet formation, involving both the BZ and BP mechanisms describe above - e.g. McKinney & Gammie (2004); Hawley & Krolik (2006).

## 2.5 M87* spin estimates

In contrast with the consensus on the mass of the black hole, a range of methods has produced widely varying results for the spin of M87*. Estimates (see summary in Table 2.1) range from low spin levels (∼0.1), to very high spin, approaching the maximum spin parameter of a=1.

| Method | Example of study using this method | Spin parameter (a) |
|---|---|---|
| Estimating the position of the jet boundary shape break | Nokhrina et al. (2019) | $\sim 0.2-0.3$ |
| Estimating the wobbling period of the accretion disk. | Sob'yanin (2018) | $0.1 < a < 0.5$ |
| Measuring the innermost stable circular orbit | Doeleman et al. (2012) | $> 0.2$ |
| Modelling the energy to power the jet | Nemmen (2019b) | $\geq 0.4$ or $\leq -0.5$ |
| Measuring the brightest point in the accretion disk. | Dokuchaev & Nazarova (2019) | $0.75 \pm 0.15$ |
| Measuring the variability of energetic TeV photons from the core. | Li et al. (2009) | >0.8 |
| Observing 'twisted light' | Tamburini et al. (2020) | 0.90±0.05 |
| Using an accretion-jet model. | Feng & Wu (2017) | $\sim 0.98$ |

*Table 2.1. Methods used to estimate M87* spin and results obtained. Source: Prepared by author.*

A brief outline of each of these studies, set out below, conveys the variety of techniques used and results obtained. It excludes the method of analysing the shape and size of the black hole shadow, given that observational results are not yet sufficiently precise, as explained in section 2.4.2.

a) Estimating spin through the position of the jet boundary shape break

Nokhrina et al. (2019) propose a new method to estimate the mass and spin of M87*, by analysing a change in the jet shape along its extension. After launching, Asada & Nakamura (2012) were the first to report that the M87 jet follows an approximately parabolic trajectory (jet width, $d \propto r^{0.5}$, where r is the distance from the core), before transitioning to a conical shape ($d \propto r$) further downstream. A similar jet boundary shape break was subsequently found in other galaxies - e.g. Hada et al. (2018), suggesting that a common jet formation mechanism may exist. This transition in jet geometry is interpreted as arising from the flow transiting from the magnetically dominated regime to the energy equipartition between plasma bulk motion and magnetic field (Nokhrina et al., 2019). The authors compare the results of observational data collected by Nakamura et al. (2018) with magnetohydrodynamic modelling of the jet structure. From investigation of the break properties, the authors estimate black hole spin, mass, and jet properties. The study reports a value for M87* mass, which aligns with the published EHT value (EHTC et al., 2019f), and predicts a moderately low spin parameter of $a \sim 0.2-0.3$.

b) Estimating the wobbling period of the accretion disk

Sob'yanin (2018) estimates the spin parameter of M87*, based on the prediction of the Kerr metric that a tilted accretion disk will change the orientation of its rotational axis. If the accretion disk does not co-align with the equatorial plane of the black hole, frame dragging will cause the accretion disk to precess. This

Lense−Thirring precession is a direct observable effect, which provides a method to estimate the black hole spin. The period is estimated at 8−10 years, based on VLBA observations at 43GHz (Walker et al., 2018). The wobbling was modelled with a test particle, generating an angular momentum, which implied a spin parameter, a, of $\sim$ 0.5±0.3 (Wilkins, 1972). However, in the more realistic case of the accretion disk precessing as a solid-body-like disc, the spin parameter was estimated as significantly smaller, with $a \sim 0.15\pm$ 0.05. Sob'yanin's method thus implies a spin parameter, a, in the range 0.1 to 0.5.

c) Measuring the innermost stable circular orbit (ISCO)

Given the relationship between spin and the location of ISCO, as discussed in section 2.4.1, the measurement of ISCO may be used to estimate both the spin rate and the direction of spin of the black hole, relative to the accretion disk.

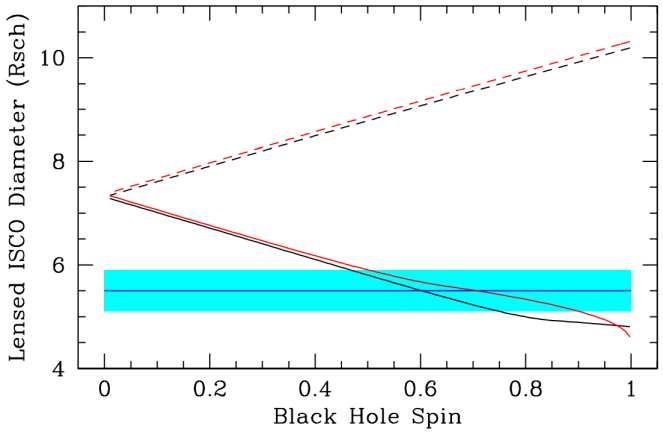


Figure 2.9: *Lensed ISCO diameter v spin parameter, a. The horizontal (blue) line indicates the results of Doeleman et al. (2012), with the level of uncertainty (± 1$\sigma$) illustrated by the width of the band. Image credit: (Doeleman et al., 2012, Figure 3)*

Doeleman et al. (2012) took into account that ISCO is enlarged, due to the strong gravitational lensing that occurs at small radii, computing the apparent diameter

of ISCO using ray-tracing algorithms. They find (Figure 2.9) that M87* has a prograde spin, with a $> 0.2$ (assuming a $3\sigma$ upper limit on the measurement of ISCO).

d) Modelling the energy to power the jet

Assuming mass accretion fuels black holes, Nemmen (2019b) estimated the spin of M87*, based on the minimum energy required to power its jet and an upper limit of the mass accretion rate. These two key observables were used to estimate jet efficiency, which was then compared with results from GRMHD jet formation models.

Nemmen's estimate of jet power was based on Chandra telescope data on the inflation of x-ray cavities from jet plasma. This technique, which estimates the energy needed to inflate the observed cavities, time averaged over a period of $10^6$ years, quantifies the jet power at $10^{36}$ $Js^{-1}$ (Russell et al., 2013). The estimated mass accretion rate onto M87* was sourced from Kuo et al. (2014), based on analysis of the polarisation of radio emission. The technique assumes that synchrotron radio emission from the inner accretion flow is subject to polarisation close to the black hole, when the polarisation plane of radio emission rotates due to magnetic flux. The study estimated an accretion rate onto M87* of $\dot{M} \geq 9.2 \times 10^{-4} M_{\odot} yr^{-1}$.

The two key observables of jet power, P, and mass accretion rate onto the black hole, $\dot{M}$, enable the jet efficiency ($\eta$) to be estimated, using $\eta = P/\dot{M}c^2$. This is a key input into a GRMHD simulation model of accretion flows onto the black hole, based on a method from Tchekhovskoy et al. (2012). The behaviour of magnetised plasmas was simulated near the event horizon, modelling jet power on the spin parameter, $a$, and magnetic flux, $\phi$ (assuming the Blandford-Znajek process). According to this model, the jet power, $P \propto (a\phi/M)^2$, where $a$ is the rotation parameter and $\phi$ is the magnetic flux threading the event horizon. The result of these simulations leads to constraints for the spin parameter of $a \geq 0.4$ or $\leq -0.5$ (see

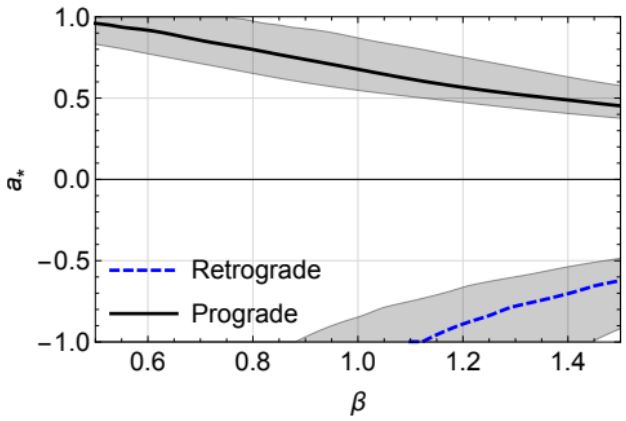


Figure 2.10: *The spin parameter, a, of M87* versus density index, $\beta$, for both prograde (continuous line) and retrograde (dashed line) spin. The shaded region denotes the level of uncertainty. Image credit: (Nemmen, 2019a, Figure 3).*

Figure 2.10).

e) Measuring the brightest point in the accretion disk

Dokuchaev & Nazarova (2019) analysed the first image of M87* from EHTC et al. (2019a) to estimate its spin. They created a model centred on the dark silhouette of the event horizon, which is smaller than the black hole shadow (see Figure 2.12). In the model, the outline of the silhouette (the image of the event horizon equator) is placed inside the expected position of the black hole shadow. The angular distance from the centre of the observed event horizon silhouette to the brightest position in the accretion disk was calculated mathematically, assuming that this point is located at $R_{ISCO}$. This was then compared with results from their analysis of the EHT image, yielding an estimate for the spin parameter, a, of $\sim 0.75 \pm 0.15$.

f) Measuring the variability of energetic $\gamma$-ray flux from the core of M87

Li et al. (2009) used the rapid variability of energetic TeV photons in the core region of M87* to constrain the spin parameter. M87* is a very-high-energy $\gamma$-ray

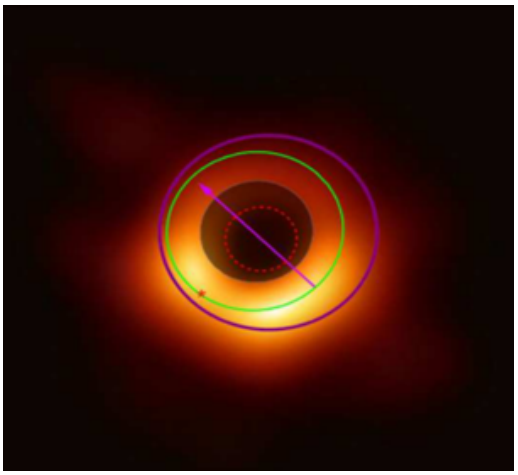

Figure 2.11: *The first M87* image from EHT, overlayed with an accretion disk model. The brightest point in the disk is marked with a red star on the modelled ISCO orbit (shown in green), while the red circle (dashed) indicates the event horizon generated by the simulation. Image Credit: (Dokuchaev & Nazarova, 2019, Figure 7)*

source and the rapid flux variability ($\sim$ 2 days) suggests a very compact TeV emission region. The extent to which $\gamma$-rays can escape from the vicinity of the black hole, an environment with high radiation density, depends on gamma-photon collisions, which may generate electron-positron pair production and absorption of the gamma-rays. The optical depth of the radiation fields near the event horizon to TeV photons due to pair productions is found to be strongly dependent on black hole spin. The authors estimate that the observed level of TeV photons escaping from the innermost region of the radiation fields from the accretion disk corresponds to a spin parameter, a $\geq 0.8$. Although Wang et al. (2008) previously used a similar technique to estimate a $\geq 0.65$, the subsequent analysis by Li et al. (2009) is more complete, as it takes account of GR effects.

g) Observing 'twisted light'

Tamburini et al. (2020) used EHT observational data gathered over four days to estimate the spin of M87*, focusing on the phase twisting of electromagnetic radiation near the black hole. The method estimated orbital angular momentum (OAM) and electromagnetic vorticity from the brightness temperature of the M87* ring. Quantitative phase information was obtained using intensity measurements and data analysis yielded the phase wavefront and OAM. The rotation parameter, $a$, was estimated to be $0.90 \pm 0.05$.

h) Using an accretion-jet model to estimate spin

Feng & Wu (2017) constrained M87* spin using an accretion-jet formation model, combined with estimates of the accretion rate near the event horizon and the power of the jet. The multi wavelength Spectral Energy Distribution of M87 was fitted with the accretion-jet model. The study used the hybrid jet formation mechanism, described in section 2.4.3, to calculate the expected jet power at different spin levels. The observed jet power of $\sim 8 \times 10^{35} Js^{-1}$ was sourced from :- Rafferty et al. (2006); Russell et al. (2013). In order to generate this observed jet power, Feng & Wu (2017) estimate a $\sim 0.98$.

## 2.6 Summary

In this Chapter, the fundamental characteristics of black holes were introduced, together with the key elements of the M87* system. The mass of M87*, one of its key characteristics, was then discussed, followed by a review of different approaches to measuring its spin. Eight different studies were outlined and the wide range of results obtained illustrates the challenge of measuring the spin parameter. The next Chapter reviews M87* research undertaken by the EHTC, which has published observational data that are used in subsequent Chapters to calculate the author's own estimates of key M87* parameters.

# Chapter 3

# The EHT Collaboration's Research on M87*

This Chapter describes the EHT instrument and provides an overview of the science behind VLBI techniques that have been developed to resolve horizon scales for M87* and other selected observational targets. It explores how the EHTC has linked radio telescopes across several countries to observe these targets and obtain vast amounts of data, which are processed and analysed using advanced image reconstruction methods. This international partnership has made possible the first images of M87*, which were published in April 2019. The success in imaging M87* represents a significant milestone in black hole physics and has spurred on further work to improve the resolving power and sensitivity of the EHT virtual Earth-sized telescope. The EHTC has now broadened its research and investigated polarised emission in the core region of M87*. The magnetic field lines have been successfully mapped, resulting in progress constraining the magnetic field structure and plasma properties close to the black hole's event horizon.

## 3.1 The EHT instrument

The EHTC's objective of forming an array of telescopes, separated by very large distances, is to obtain an angular resolution from Earth sufficient to image a black hole. If we consider the angular resolution, $\theta$, of a single radio telescope, this can be estimated from the formula, $\theta \sim \lambda/D$, where $\lambda$ is the incoming radio wavelength being observed and D is the diameter of the radio dish (Wilson et al., 2013). Given the objective of maximising angular resolution, this relationship clearly conveys the importance of maximising D and/or minimising $\lambda$. This dependency may be illustrated by comparing relative resolving power between optical telescopes and radio dishes. As the latter operate at long wavelengths, compared to optical instruments, it is apparent that they must be relatively large to achieve the same resolution. For example, let us assume that the Large Millimeter Telescope, which is the largest telescope in the EHT array, has a diameter of 50m and operates at a wavelength of 1.3mm. The telescope thus has a resolving power of $\theta = (1.3 \times 10^{-3})/(50) = 2.6 \times 10^{-5}$ radians. By way of comparison, an optical instrument operating at a typical wavelength of, say, 500nm, would need a diameter of only $(500 \times 10^{-9})/(2.6 \times 10^{-5})$ ∼2cm to achieve a similar resolution.

In order to match the size of the emission ring of M87*, the resolving power of the EHT instrument has to be $\sim 25\mu as$ (EHTC et al., 2019a), which is equivalent to $1.2 \times 10^{-10}$ radians. The diameter of a single telescope with this resolving power can be estimated, assuming an operating wavelength of 1.3mm, as D = (wavelength ($\lambda$))/(ang resolution (radians)) = $(1.3 \times 10^{-3})/(1.2 \times 10^{-10}) = 10,800$km. As this size is clearly not realistic, a solution was developed to obtain an equivalent resolution by using an array of radio dishes located strategically around the Earth. Using aperture synthesis, which has proved to be a breakthrough technique in interferometry, inputs from a collection of radio dishes are combined together to synthesise a large effective aperture. This virtual telescope emulates the outcome from a single

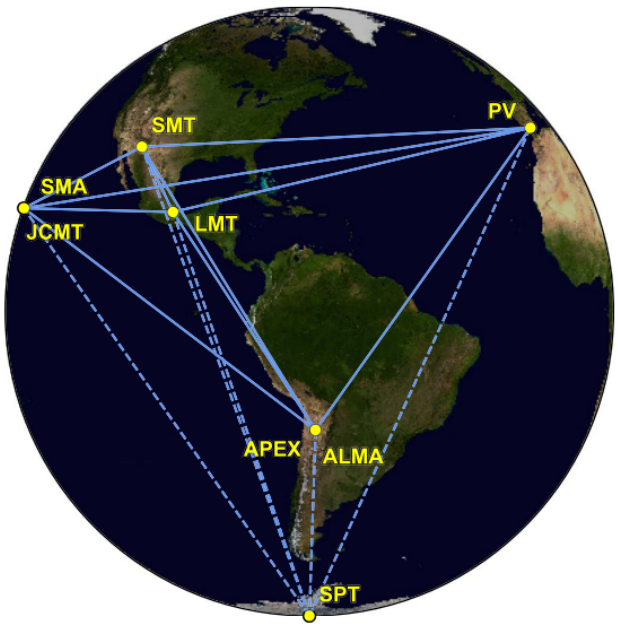


Figure 3.1: *Telescopes used in EHT's 2017 programme to image M87* and Sgr A*. Eight observing stations were used across the six different marked locations. Image credit: EHTC et al. (2019a), Figure 1.*

telescope, having a similar diameter as the length of the array's baseline. It creates an aperture similar to the distance between the two dishes in the array that are furthest apart and these dishes are synchronised to carry out simultaneous observations of the same target.

In the EHT 2017 observational campaign, eight radio telescopes were used in different geographical locations to form an array around the world, as illustrated in Figure 3.1. The baseline lengths in this configuration range from 160m to 10,700km (EHTC et al., 2019a). As explained above, the longest baseline was thus, in principle, sufficient to resolve the core of M87*.

## 3.2 The principles of Very Long Baseline Interferometry (VLBI)

In this section, we consider in more detail the VLBI technique, which is used with an array of radio dishes that operate together as one virtual telescope. The principles are explained by using an illustration of a simple two element radio interferometer arrangement (see Figure 3.2).

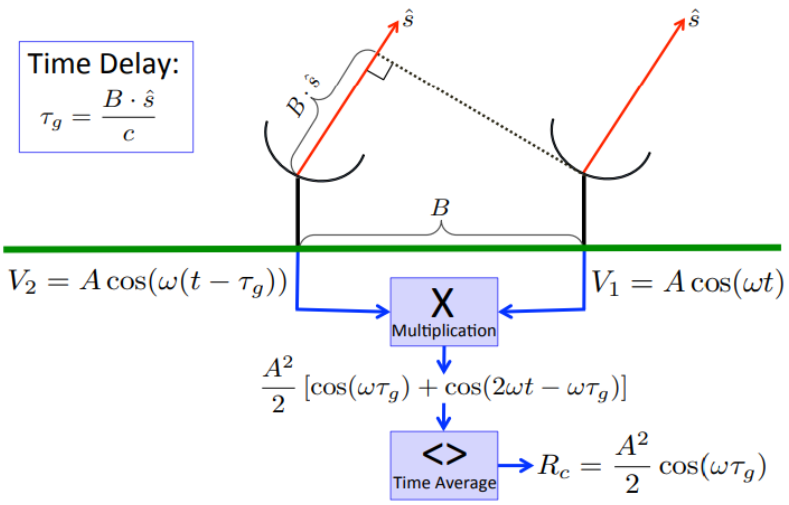


Figure 3.2: *Simplified interferometry diagram. Image credit: Bouman et al. (2016), Figure 2.*

Let us assume that an emission from a distant radio source at frequency, $\nu$, arrives at the interferometer from direction $\hat{s}$. While each of the two dishes is targeted at the same object in the sky, radio waves from the source reach the nearer dish (right-hand side of Figure 3.2) at a time, $\tau_g$, before the second dish. As the two antennas are distance B apart, the emission travels an extra $B \cdot \hat{s}$ to reach the latter detector, resulting in a time lapse between both signals of $\tau_g = B \cdot \hat{s}/c$, which depends on the source's position in the sky. The radio dishes measure the electric field from the source, converting it into a voltage that is processed electronically. We also assume

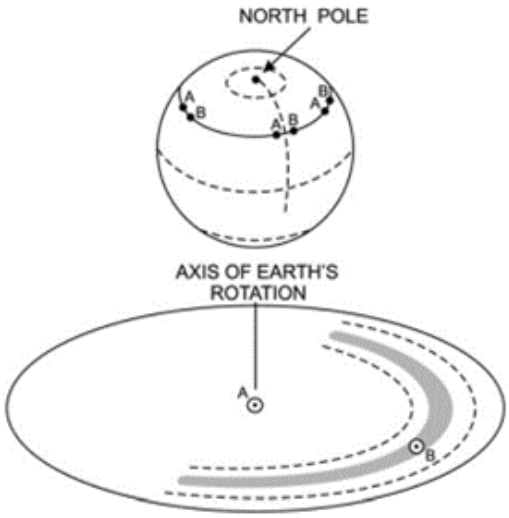


Figure 3.3: *Diagram illustrating an array which has two dishes (A and B) along a baseline from East to West. Image Source: (Wilson et al., 2013, Figure 9.7).*

that the voltages produced at the two radio dishes, due to the electric field from the source, are $V_1$ and $V_2$ respectively. Let the voltage at the nearer dish be $V_1 = A\cos(\omega t)$, where $\omega = 2\pi\nu$. Taking into account the time delay, the voltage at $V_2 = A\cos(\omega(t - \tau_g))$. Signals received by both dishes are channelled into a correlator, which multiplies and averages the input data. The time averaged correlation of the recorded signals is a sinusoidal function, with limited information on the source position.

For a simple array comprising two dishes, the signal path for the radio source received from a distant object, such as M87*, will move in phase and out of phase during a period of observation, as the Earth rotates. Over time, the phase differences arising from the changing distance to the radio source from each antenna create interference fringes. The fringes from each pair of antennas represent the "brightness" profile of the radio source. In Figure 3.3, an array with two dishes (A and B) is shown, along an East to West baseline. The array tracks the target and, as the Earth rotates, the array moves its position relative to the target, enabling

large numbers of interferometer pairs to be sampled during an observation period. While a two-dish interferometer generates spatial information along only one direction, in practice arrays of antennas are assembled to provide data across different orientations. As the number of $(u, v)$ samples is increased, the quality of the final image and, therefore, our understanding of the source structure, will improve. As the Earth rotates, each pair of dishes gathers data on different spatial orientations, which are then linked together. For example, the Very Large Array in New Mexico comprises 27 separate radio dishes, which can be linked to represent $27 \times 26 \ / \ 2 = 351$ spatial frequencies measured from interferometer pairs.

The EHT instrument measures complex 'visibilities' on a variety of baselines $B_{ij}$, between widely separated radio dishes, i and j (EHTC et al., 2019f). An interferometric visibility is a Fourier component of the source brightness distribution. Each visibility is unique to a baseline length and orientation. The key concept behind the technique is that the image (which is the intensity distribution of the target source) has a Fourier transform, which is the two-point correlation function of the electric field, whose components (or 'visibilities') can be directly measured (Thompson et al., 2017).

The van Cittert–Zernike theorem is at the heart of aperture synthesis and crucial to the measurement of the brightness distribution of a source (Thompson et al., 2017). The complex visibility, $\Gamma_{i,j}(u, v)$, is the Fourier transform of the intensity distribution function of a distant, spatially incoherent source. The theorem states that the correlation of signals received by two radio dishes, i and j, for a wavelength, $\lambda$, is approximately

$$\Gamma_{i,j}(u, v) \approx \int_{\ell} \int_{m} e^{-i2\pi(u\ell+vm)} I_{\lambda}(\ell, m) d\ell dm, \tag{3.1}$$

where $I_{\lambda}(\ell, m)$ is emission with wavelength $\lambda$ from direction $\hat{s} = (\ell, m, \sqrt{1 - \ell^2 - m^2})$. The coordinates $(u, v)$ are the projected baseline, B, orthogonal to the line of sight.

As the spatial frequency, $(u,v)$, is proportional to the distance between the radio dishes, B, it can be seen that an increase in B will enhance the resolving power of the telescope.

Formula 3.1 is essentially the Fourier transform of $I_\lambda(\ell, m)$, the source emission image. $\Gamma_{i,j}(u, v)$ represents a single complex Fourier component of $I_\lambda$ at position $(u, v)$ on the spatial frequency plane. The Fourier inversion of this equation leads to:

$$I_\lambda(\ell, m) \approx \int_u \int_v e^{i2\pi(u\ell+vm)} \Gamma_{i,j}(u, v) du dv \tag{3.2}$$

Measurement of the visibility function, $\Gamma$, thus enables the brightness distribution, $I_\lambda(\ell, m)$, to be obtained. As each point on the $(u,v)$ plane samples one component of the Fourier transform of the brightness distribution, our knowledge of the source structure becomes more detailed and complete as the number of $(u,v)$ samples is increased (EHTC et al., 2019c). The corollary is that, if all Fourier components of the source brightness distribution are not sampled, some information on the source will therefore be missing.

The importance of coverage is illustrated in Figure 3.4, which indicates the locations in the $(u,v)$ plane which record data from the target. In this example, the array comprises three instruments, with A paired with B and A linked with B1. The grid shows black areas on the $(u,v)$ plane which have gathered data and blank zones, which denote missing data on the source. The telescopes sample and record data from the target source, which are synchronised with a high level of accuracy (tens of nanoseconds) using the Global Positioning System (EHTC et al., 2019b). In order to operate at a wavelength of 1.3mm, technical challenges must be addressed, such as noise from radio receivers, atmospheric opacity and lower efficiency of the telescopes. Since early VLBI experiments to study M87*, array sensitivity has been increased by a factor of $\sim 30$, enabling a theoretical resolution of $\sim 25\mu as$ to be achieved (EHTC et al., 2019c).

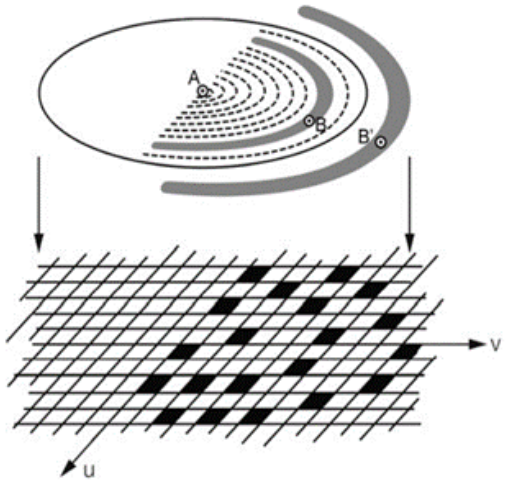


Figure 3.4: *Sketch of the* u,v *plane, indicating data from three dishes (A, B and B1) on a baseline. Source: Figure 9.8 in Wilson et al. (2013).*

## 3.3 Imaging M87*

The aggregated (*u,v*) coverage over four days of observations in April, 2017, is shown in Figure 3.5, which indicates the different pairs of dishes, e.g. JCMT-LMT, at the participating locations. The programme of observations comprised between seven (April 10) and 25 scans (April 6), with the duration of each scan varying from three to seven minutes (EHTC et al., 2019b). Measurements correspond to elliptical tracks in the spatial frequency plane of the target. The frequencies (*u,v*) are the baseline lengths orthogonal to the line of sight from each pair of dishes (Bouman et al., 2016). As illustrated in Figure 3.4, limited sampling of the (*u,v*) plane leaves significant gaps in coverage and presents challenges in reconstructing images of the target.

A one-dimensional radial cut of the visibility amplitudes from April 11, 2017 through the Fourier plane, averaged over 360°, is set out in Figure 3.6. Measurement of this data enables the brightness distribution to be estimated, through a Fourier transform. Given that each point in the (*u,v*) plane samples one component of the Fourier transform, the final image of the brightness distribution depends on

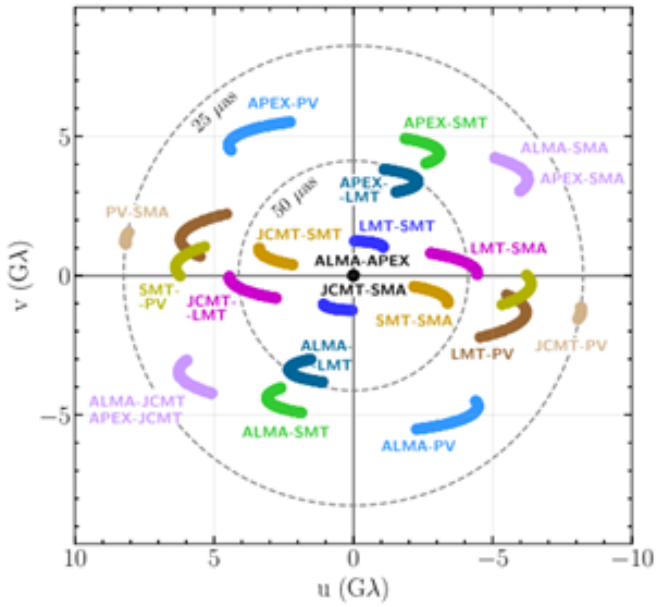


Figure 3.5: *Aggregated* (u,v) *coverage for the April, 2017 observations. The coordinates for pairs of radio dishes are shown in units of* $\lambda$ *(wavelength of observations). Dotted circular lines indicate baseline lengths for fringe spacings of* $50\mu as$ *(inner ring) and* $25\mu as$ *(outer ring). Image credit: EHTC et al. (2019a), Figure 2 (top).*

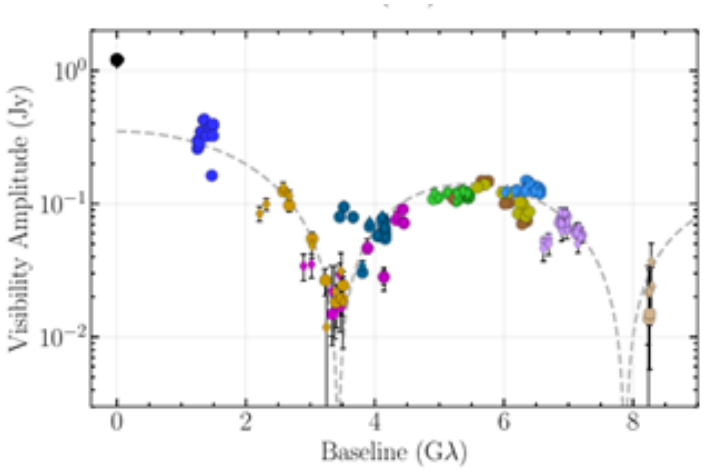


Figure 3.6: *Final visibility amplitudes (Jy) v length of baseline. Produced from April 11, 2017 observations. Image credit: EHTC et al. (2019b), Figure 2 (bottom).*

the number of samples obtained. The dashed line in Figure 3.6 traces the Fourier transform of a thin ring model with a diameter of 46 µas and facilitates comparison with the data. Extensive image reconstruction was required to obtain a final image from this data (EHTC et al., 2019a), as explained in the following section.

## 3.4 Data processing, imaging and analysis

Each radio dish in the array is connected to a data handling unit. Given the separation between telescopes, the large amounts of data recorded at each station ($\sim 64$ Giga-bits per second) are initially retained at each location. Disk packs are subsequently transported to a central data hub for correlation and analysis. Data processing is a critical step that involves key challenges, such as ensuring very stable recordings, which enable precise measurement of phase differences. Extremely accurate hydrogen masers are used to time stamp the data, which is synchronized to within tens of nanosecond using the Global Positioning System (EHTC et al., 2019a).

The final phase is to reconstruct images from the data. This represents a further challenge, given the availability of data on a relatively small number of points on the $(u,v)$ plane and large amplitude calibration uncertainties. In order to address these obstacles, robust computational algorithms have been developed and enhanced for EHT research, to reconstruct images from these incomplete measurements (EHTC et al., 2019d). The methods used incorporate assumptions and constraints that generate results which provide the optimum fit for the observational data (Bouman et al., 2016). In the EHT analysis of M87* data, CLEAN and Regularised Maximum Likelihood (RML) image synthesis algorithms were used. As these statistical techniques require manual intervention, four teams worked independently, using different methods, in order to produce images without the risk of human bias (EHTC et al., 2019a).

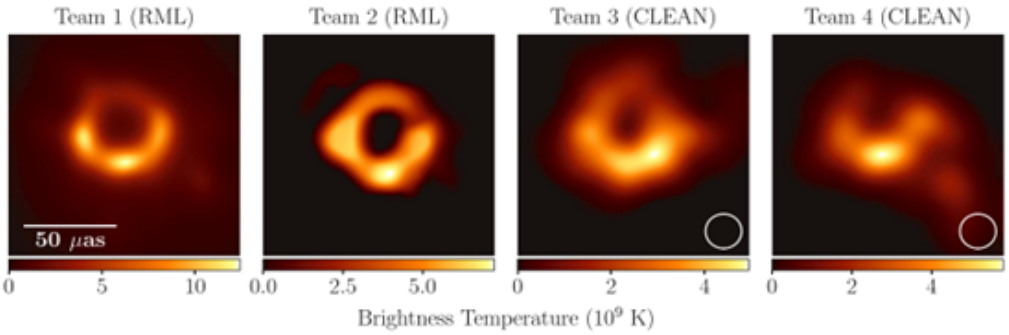


Figure 3.7: *Images produced by independent teams from data obtained during observations on April 11, 2017. Image Source: EHTC et al. (2019d), Figure 4.*

The CLEAN method is a well-established deconvolution technique used in radio interferometry for image reconstruction from incomplete data (Wilson et al., 2013). The algorithm, which is based on the assumption that the original image can be represented by the superposition of point sources, has an iteration phase, followed by a reconstruction phase. The point in the initial "dirty" image with the highest value is found and a scaled point spread function (PSF) is subtracted. The process is repeated until a noise threshold is reached. Then the "clean" image is "reconstructed" by building up the subtracted PSFs onto a blank image. The result is an image that is "cleaned" of noise (Thompson et al., 2017). Regularized Maximum Likelihood (RML) was also used to generate images (EHTC et al., 2019d). This algorithm seeks to produce a physically plausible image that aligns with the data and has specified properties eg smooth or compact, although it also involves an element of self-calibration (EHTC et al., 2019a).

In the M87* image reconstruction, the four independent teams were brought together to compare results and collaborate on the final stages of the exercise. The four initial images produced are shown in Figure 3.7, with teams 1 and 2 working on RML and teams 3 and 4 using CLEAN. Although the four images are consistent in showing an asymmetric ring of $\sim 40\mu$as, which is brighter in the south, the ring thickness and brightness temperature varies between these results. The last stage of

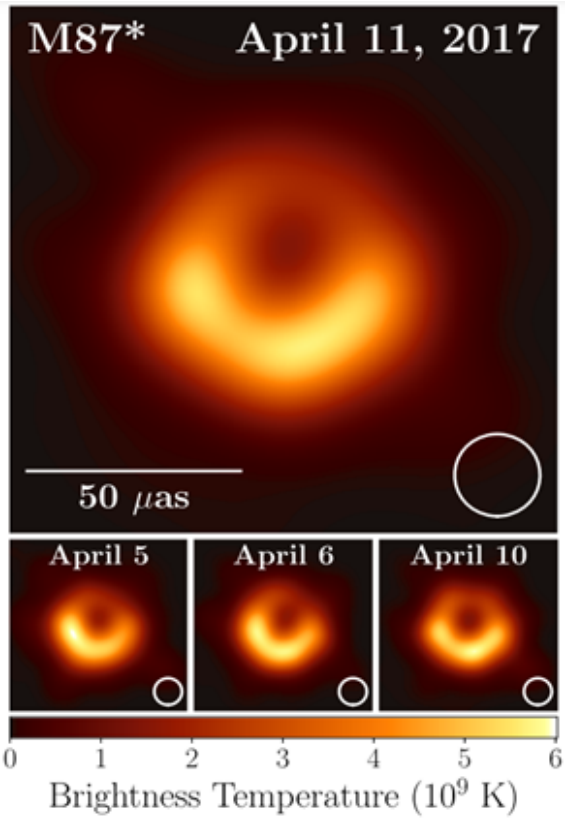


Figure 3.8: *Top: M87* image from observations on April 11, 2017 (shown in units of brightness temperature). Bottom: similar images taken over earlier days, showing the stability of the basic image structure and the equivalence among different days. Image Source: EHTC et al. (2019a), Figure 3.*

analysis involved three imaging workstreams, which used different software packages to generate images. A set of parameter combinations was selected that produced M87* images closely fitting the data and also good results from synthetic data for selected shapes (eg ring, crescent and filled disk). The output consistently produced images showing an asymmetric ring, with a diameter of $\sim 40\mu as$, although variations arose in other aspects, explained by differences between the angular resolution of the different methods. Finally, the image of M87* for April 11, 2017 (see Figure 3.8) was produced by averaging the results of the three different reconstruction methods. The lower section of Figure 3.8 sets out three similar images taken in the

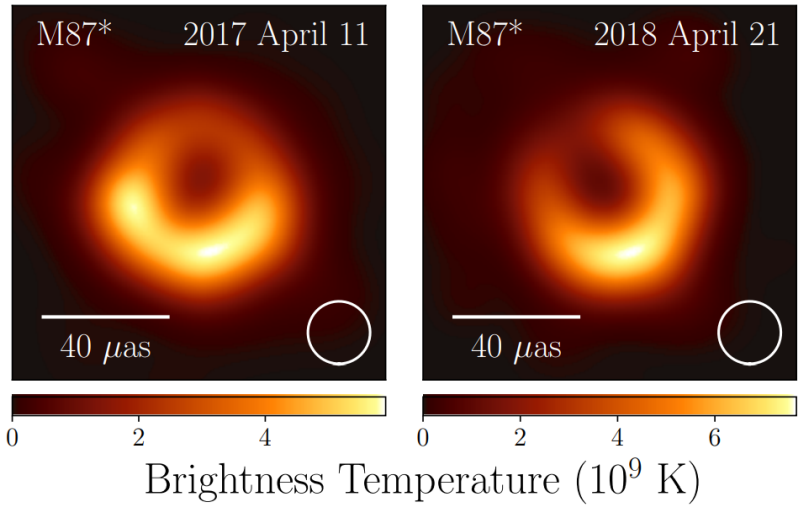


Figure 3.9: *Images of M87* from observational programmes in 2017 and 2018 (left and right-hand images respectively). A comparison of these images, separated in time by approximately one year, shows consistency in diameter and location of peak brightness, although there is a clear shift in the position angle of the brightness asymmetry. Image Source: EHTC et al. (2024), Figure 1.*

week before April 11, which suggests that the target structure is relative stable over this timescale.

## 3.5 2018 observation campaign

Since the first observations in April 2017, images from data obtained one year later, in April 2018, have been published (EHTC et al., 2024). The second observing programme benefitted from an improved array, with additional baselines from the Greenland Telescope providing better $(u, v)$ coverage, particularly North to South. The new observations reveal a similar, bright emission ring (see Figure 3.9). Obtaining these two sets of observations, separated by a year, confirmed the consistency of the shadow's size and shape. For example, the diameter of the 2018 ring was measured as $43.3\mu$ arcsec, which was similar to the 2017 ring (EHTC et al., 2024). The

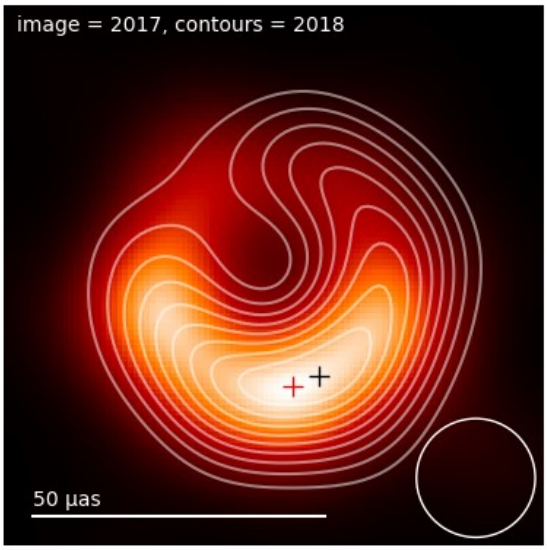


Figure 3.10: *M87* image from the 2017 observing programme, overlaid with brightness contours from 2018 image. The peak brightness in 2017 (red cross) and 2018 (black cross) are located to within a quarter of one beam (white circle). Image Source: Paper by Drew et al. (2024), currently under peer-review.*

ability to reproduce these results is a key milestone for the EHTC, as the consistency of the results from 2017 to 2018 supports the case that the observations represent strongly lensed emission from a black hole, as predicted by general relativity. As the radius of the black hole is dependent on its mass and M87* does not have a high accretion rate, e.g.: Kuo et al. (2014), suggesting that its radius will change very slowly over human timescales.

Although the ring size and morphology are similar to the 2017 observations, the 2018 data also reveals differences from the earlier epoch. A striking change between the two images is the extent of the bright region, which has become smaller during the period between observations. In addition, the brightest region of the ring has shifted by $\sim 30°$. This unambiguous confirmation of movement in the position angle of the brightness asymmetry in the disk suggests that the disk is a turbulent accretion environment. The finding supports a previous study, which had insufficient data

to produce images, but used simple geometric models to identify a marked change between the position angle measured in 2013 and 2017 (Wielgus et al., 2020).

Figure 3.10 shows the 2017 image, overlaid with the 2018 brightness contours. The crosses, which indicate the peak brightness for 2017 (marked in red) and 2018 (black), have not moved significantly. The location of peak brightness is consistent to within a quarter of a beam width (noting that the crosses do not represent error-bars). It is hypothesised that the brightest spot (that remains static) arises from the relativistic rotation of the disk, while the enhanced brightness on one side of the disk is explained by relativistic beaming. The reduced region of brightness in the image may be explained by a range of factors, including turbulent movement of plasma in the disk and changes in the location and relative brightness of the base of the jet.

## 3.6 Polarisation measurements

As a further stage in its investigation of M87*, the EHTC produced the first polarised images around the black hole in 2021 (EHTC et al., 2021a). These polarimetric results complement total intensity images and are a powerful research tool, carrying information relating to the magnetic fields close to the black hole, that drive the synchrotron emission.

The EHT results suggest that a significant proportion of the light around M87* is polarised, although the fractional linear polarisation appears to be highest ($\sim 15\%$) in the southwest quadrant of the ring structure (see Figure 3.11). An alternative visualisation scheme for the polarimetric image of M87*, from April 11, 2017 observations, is shown in the form of a tick plot in Figure 3.12. The ticks illustrate the direction and level of linear polarisation, while the tick colour records the amplitude of the polarisation.

Polarised synchrotron radiation traces the underlying magnetic field structure

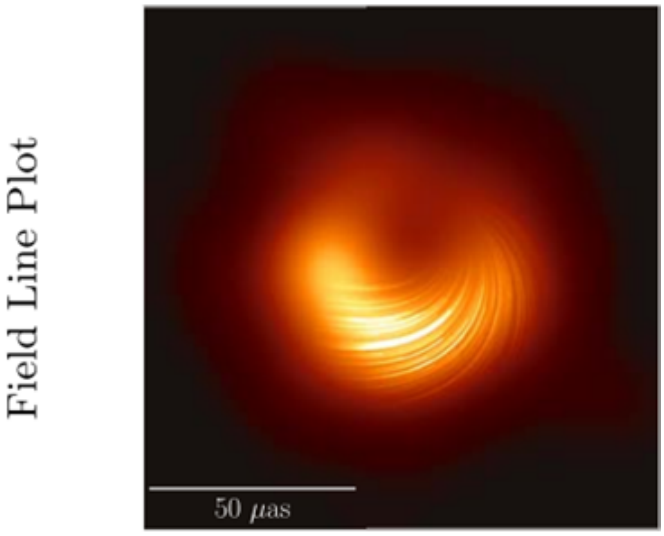


Figure 3.11: *Polarisation 'field lines' around M87*, plotted on image of underlying total intensity. Image produced by averaging results from April 5, 2017 observations, using five different reconstruction methods. Image source: (EHTC et al., 2021a, Figure 7).*

along the line of sight (Mościbrodzka et al., 2017). If this radiation passes through a magnetized plasma, the plane of polarisation will rotate. This Faraday rotation is dependent on the wavelength and the rotation measure (RM) may be estimated from

$$RM = \frac{\chi(\lambda_1) - \chi(\lambda_2)}{\lambda_1^2 - \lambda_2^2}, \tag{3.3}$$

where $\chi$ is the position angle of the polarisation plane and $\lambda_1$ and $\lambda_2$ are two observed wavelengths that are close to each other. In the EHTC study, the change in $\chi$ was measured at four different frequencies, in order to estimate the Faraday rotation (RM) associated with the M87 accretion flow.

Measurement of the observed polarisation of radiation in the radio emission, assuming that it is polarised by the inner accretion flow as it travels towards the observer, enables several important parameters of M87* to be estimated. Using this approach, the EHTC estimated an average emission region plasma density of

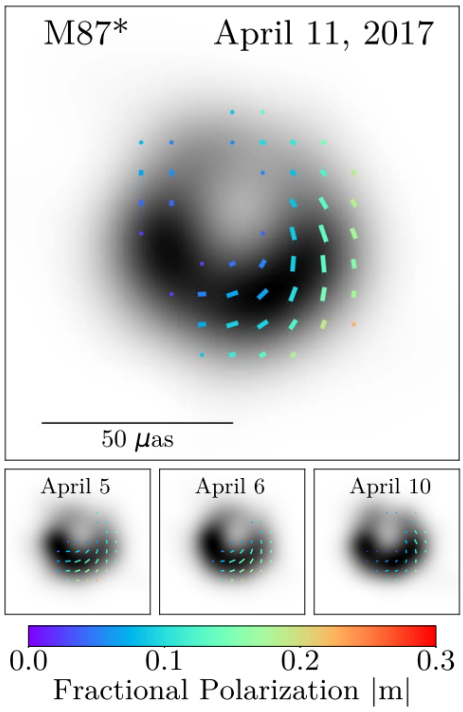


Figure 3.12: *Top panel: Polarimetric image of M87* from April 11, 2017 observations. The ticks illustrate the direction and level of linear polarisation. Bottom panel: Polarimetric images obtained on earlier dates during the observational programme. Image source: EHTC et al. (2021a), Figure 1.*

$n_e \sim 10^4$ to $10^7 \mathrm{cm}^{-3}$, magnetic field strength of $B \sim 1$ to 30 G, and electron temperature $T_e \sim$ (1 to 12) $\times 10^{10}$ K (EHTC et al., 2021b). GRMHD simulation models were used by the EHTC to infer a mass accretion rate onto M87* of $\dot{M} \sim$ (3 to 20) $\times 10^{-4}$ $M_\odot$ $\mathrm{yr}^{-1}$, based on the estimated RM of the M87 core $\sim 5 \times 10^5$ $\mathrm{radm}^{-2}$. This result is in line with earlier work by Kuo et al (2014), who estimated the RM to be between $-7.5 \times 10^5$ $\mathrm{radm}^{-2}$ and $3.4 \times 10^5$ $\mathrm{radm}^{-2}$ and the mass accretion rate $\dot{M} < 9.2 \times 10^{-4} \mathrm{M}\odot yr^{-1}$.

## 3.7 Summary

This Chapter outlined the EHTC initiative, which has successfully exploited VLBI techniques to resolve horizon scales for M87*. Apart from significant improvements to the EHT array, this achievement required advances in data processing, imaging and analysis techniques. The breakthrough led to publication of the first images of M87*, followed by polarisation images around the black hole. Analysis of the 2018 data revealed a similar image to the previous year, confirming the consistency of the shadow size and shape. However, the bright region moved about 30° counter-clockwise, although the author's analysis indicates that the brightest spot remained static. The next Chapter sets out a new method developed by the author to estimate the spin parameter of M87*, using EHT data.

# Chapter 4

# New estimate for M87* spin

## 4.1 Introduction

A range of methods have been used in different studies to measure the M87* spin, resulting in very different outcomes. In Chapter 2, the techniques used in eight estimates were outlined and the range of results obtained, from a $\sim$ 0.1 to 0.98, clearly conveys a lack of agreement on the level of spin. Methods include measuring the radius of ISCO and discerning the shape and size of the black hole shadow, which are both theoretically linked to the spin parameter. Other approaches analyse the energetics of the black hole system, which drives its relativistic jet.

Given that spin and mass are the two main characteristics of a black hole, the absence of agreement on the M87* spin is in stark contrast with the consensus regarding its mass. This uncertainty motivated the author to investigate ways to measure spin and contribute to research on this important topic, by setting out a new method to constrain the spin parameter. The method uses imaging results from the EHT and is based on some important assumptions and simplifications. The result is compared with published estimates for the M87* spin from other studies and considered in the context of findings for other SMBHs.

## 4.2 Method

In this Chapter, the author measures the spin and rotation of the black hole M87*, using the following method.

### 4.2.1 Estimate the rotational velocity of the inner disk

The first step is to estimate the rotational velocity of the inner accretion disk. This is obtained by analysing observational data and ascribing the asymmmetry of brightness in the rotating accretion disk to relativistic Doppler beaming. This Doppler beaming effect is clearly visible in the EHT image of M87* (see Figure 4.1). As the accretion disk spins, on one side the fast-rotating plasma approaches Earth and, on the other side, it is moving away (EHTC et al., 2019a).

The Doppler beaming effect is observed in a range of other situations in as-

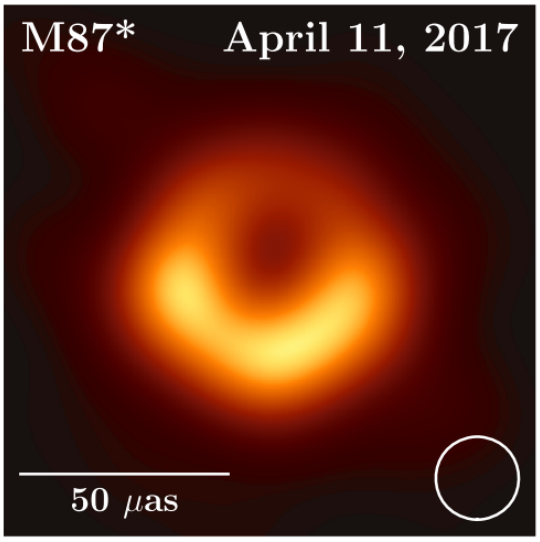


Figure 4.1: *M87* image from EHT observations (April 2017), which illustrates the approaching (southern) and receding (northern) plasma flow. Image credit: (EHTC et al., 2019b, Figure 3).*

trophysics, for example, when jets travel at high velocities close to the speed of

light. A combination of Doppler shift and photon concentration (beaming) leads to an enhancement of the observed brightness of such objects moving towards the observer and a corresponding reduction in brightness when receding. The diagram in Figure 4.2 visually captures this concept. A source of light is moving at relativistic speed towards an observer. Around the moving source, the beaming effect creates a narrow cone in the direction of motion. The observed light appears more intense as the radiation is compressed into a narrower cone. This increases the photon density reaching the observer which, combined with the higher photon energy, results in an observed increase in intensity.

The change in the source strength and frequency, as the source moves towards the observer, can be quantified. A study of intensity changes in the Doppler effect by Johnson & Teller (1982) shows that the source strength divided by the cube of the frequency is Lorentz invariant. This means that it is unchanged by a Lorentz transformation i.e. the same, regardless of the observer's inertial frame. An approaching jet or beam at a particular spectral colour would appear to emit at a combined factor of $D^3$ times brighter, where D is the Doppler factor. This comprises two factors: a frequency D times higher and into a solid angle $D^2$ times smaller (Meier et al., 2001a).

In relation to the M87* accretion disk, it is assumed that the intensity of the emitting source increases by a factor $(D_{app}/D_{rec})^3$, where $D_{app}$ is the factor for approaching matter and $D_{rec}$ for receding matter, because the emission is in a narrow frequency band and therefore $\nu \sim$ constant. This is justified, given that EHT observations at 1.3mm were conducted at a relatively narrow 4GHz total bandwidth, compared to the estimated relativistic Doppler shift of $\sim$40GHz (Chael et al., 2023).

For the purposes of the spin estimate, it is assumed that the brightness asymmetry results entirely from this beaming effect. As shown in Figure 4.3, a comparison of the 2017 and 2018 M87* images indicates a shift in the position angle of brightness


Figure 4.2: *An illustration of relativistic Doppler beaming. Image credit: Prepared by author.*

asymmetry. However, the author's analysis shows that the amount of movement of peak brightness during this period is insignificant, compared to the beam size. The consistent location of peak brightness provides confidence that it is a permanent bright spot arising from beaming, rather than another effect, such as a lump in the disk.

The Doppler factor measures the strength of the relativistic Doppler beaming, taking into account the angle between the direction of motion of the matter and the line of sight (Narayan & McClintock, 2005). In this case, we use the equation for the Doppler factor to estimate the velocity (Johnson & Teller, 1982), by comparing the difference in brightness of the approaching ($D_{app}$) and receding ($D_{rec}$) matter, as follows

$$D_{\mathrm{app}} = \left[\gamma\left(1 - \frac{v\cos\theta}{c}\right)\right]^{-1} \tag{4.1}$$

and

$$D_{\mathrm{rec}} = \left[\gamma\left(1 + \frac{v\cos\theta}{c}\right)\right]^{-1} \tag{4.2}$$

where $v$ is the velocity of the matter and $\gamma$ is the Lorentz factor, which is given by $(1 - v^2/c^2)^{-1/2}$.

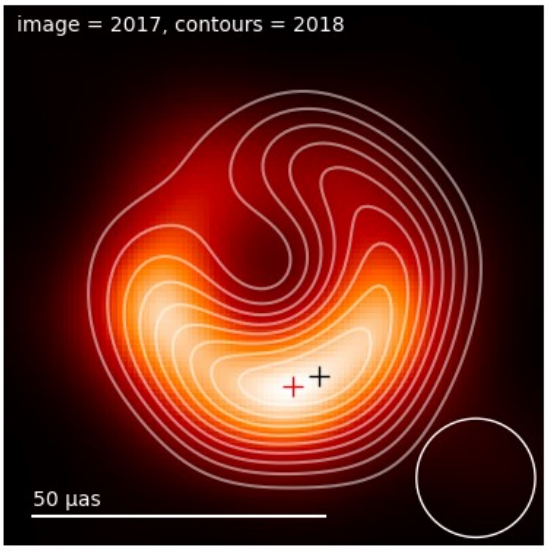


Figure 4.3: *M87* image from the 2017 observing programme, overlaid with brightness contours from 2018 image. Illustrates the proximity of the peak brightness in 2017 (red cross) and 2018 (black cross). Image Source: Paper by Drew et al. (2024), currently under peer-review.*

### 4.2.2 Estimate the radius of the innermost stable circular orbit ($R_{ISCO}$)

Following calculation of the rotation of the accretion disk using the above method, the next step is to estimate the radius of the inner edge of the accretion disk (illustrated in Figure 2.4). Differential rotation is expected across the disk, as the speed of rotation decreases further from the inner disk. It is assumed that the inner edge of the accretion disk is at the innermost stable circular orbit (ISCO), with radius $R_{ISCO}$ (Reynolds, 2021c). From a review of the literature, this assumption regarding the location of $R_{ISCO}$, the smallest marginal stable orbit, is made in several other black hole studies e.g. - Shakura & Sunyaev (1973); Li (2004); Brenneman & Reynolds (2006). In addition, the x-ray reflection spectroscopy method, which has been used in several studies to estimate SMBH spin (Reynolds, 2013), is based on

a similar assumption.

It is also assumed that the emission is all arising from the inner accretion disk, with no significant amount of matter between this and the event horizon. It is acknowledged that some GRMHD simulations predict emission from further in, as referred to in EHTC et al. (2019a), but this remains subject to debate. In any case, it is assumed that there is a very low density inside $R_{ISCO}$, thereby conserving angular momentum. As this implies relatively little material inside $R_{ISCO}$, viscosity can be ignored in this region.

In this study, the published results from three different methods are used to obtain an average value for $R_{ISCO}$ to use in the spin estimate. The methods outlined are by Doeleman et al. (2012), Dokuchaev & Nazarova (2019) and Medeiros et al. (2023). Comparison between the results from each study indicates that they are in close agreement, which justifies using the average of only three published estimates to obtain a value for $R_{ISCO}$.

Following estimates of the angular rotation rate, $V_R$, and the radius of the inner edge of the accretion disk, $R_{ISCO}$, the spin parameter, a, is calculated using the published estimate for $M_{BH}$, which is well constrained. The calculations to estimate $V_R$ and $R_{ISCO}$ are outlined in sections 4.3 and 4.4 respectively, following which the calculation of the spin parameter is set out in section 4.5.

## 4.3 The rotation of the accretion disk

As explained in the previous section, we use the equation for the Doppler factor, $D$, for both the approaching and receding sides of the disk, in order to estimate $V_R$. The angle of inclination between the direction of motion of the matter and the observer's line of sight, $\theta$, is approximately 17° (EHTC et al., 2019f). The estimated uncertainty of ±3° (Walker et al., 2018) is ignored in this calculation, noting that it

introduces an error of $< 2\%$ to $\cos\theta$. This gives

$$D_{\text{app}} = \left[\gamma\left(1 - \frac{0.96V_R}{c}\right)\right]^{-1} \tag{4.3}$$

$$D_{\text{rec}} = \left[\gamma\left(1 + \frac{0.96V_R}{c}\right)\right]^{-1} \tag{4.4}$$

Measurements of the relative brightness difference between the approaching and receding sides of the disk were obtained from published EHT data. Initially, an approximation of this difference in brightness was estimated from Figure 4.4, which

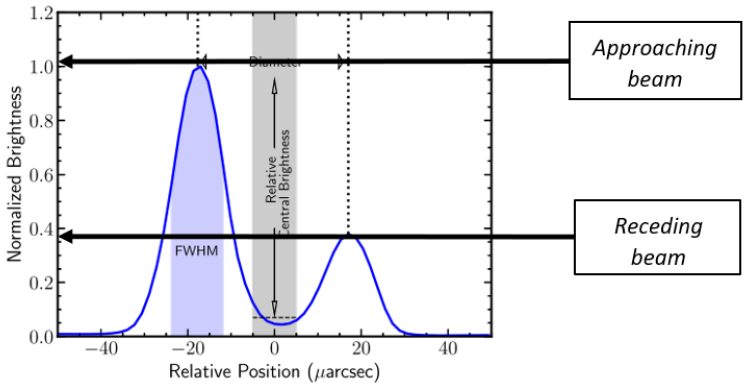


Figure 4.4: *A cross section of brightness vs relative position of each side of the ring ($\mu$arcsec). Image credit: (EHTC et al., 2019f, Figure 14), amended by the author to show the peak intensities of the approaching and receding sides of the disk.*

.

shows a cross-cut diametrically through the brightest part of the ring, normalised to the brightest portion (EHTC et al., 2019f). From measurement of the two peaks on this graph, the ratio of the intensities of the approaching and receding sides of the disk is $\sim 2.5$. However, as Figure 4.4 is a schematic diagram of relevant parameters, a more accurate figure was obtained by analysing the actual data on the brightness profiles used to construct the M87 image, which is set out in EHTC et al. (2019d), Figure 37.

The brightness profiles from three different imaging libraries are shown in Figure 4.5. An analysis of this data was undertaken, assuming Gaussian profiles, and the

output of this computation (using Maple programming) is set out in Figure 4.6. The relevant parameters estimated were the maximum amplitude and area under curve out to full-width at half maximum (FWHM). The averages of these parameters are:
Average of maxima:= 2.1 ±0.1
Average of area ratios := 2.4 ±0.25

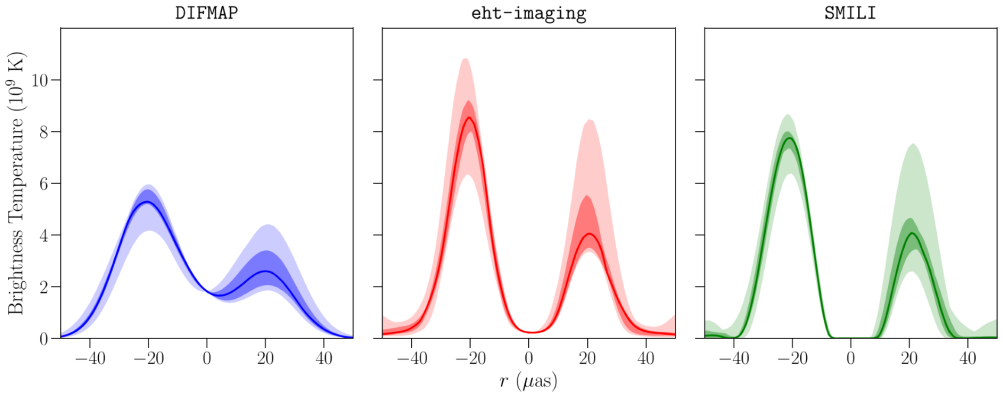


Figure 4.5: *One dimensional radial brightness profiles of the M87 images from April 11 for three imaging libraries (DIFMAP, eht-imaging and SMILI). Image credit: EHTC et al. (2019d), Figure 37.*

An average of these two values is $2.25 \pm 0.15$, which is used as the most appropriate measure of relative brightness. It is of note that this is approximately 10% less than an estimate from the diagram in Figure 4.4, although likely to be more accurate, as it is based on actual EHT data.

From the above estimate, the ratio of the intensities of the approaching and receding sides of the disk is given by $(D_{app}/D_{rec})^3 \sim 2.25$. From the equations for the Doppler factor, D, relating to the approaching (equation 4.3) and receding (equation 4.4) beams, we can derive $V_R$ from the following.

$$\left[\gamma\left(1-\frac{0.96V_R}{c}\right)\right]^{-3} = 2.25\left[\gamma\left(1+\frac{0.96V_R}{c}\right)\right]^{-3}. \tag{4.5}$$

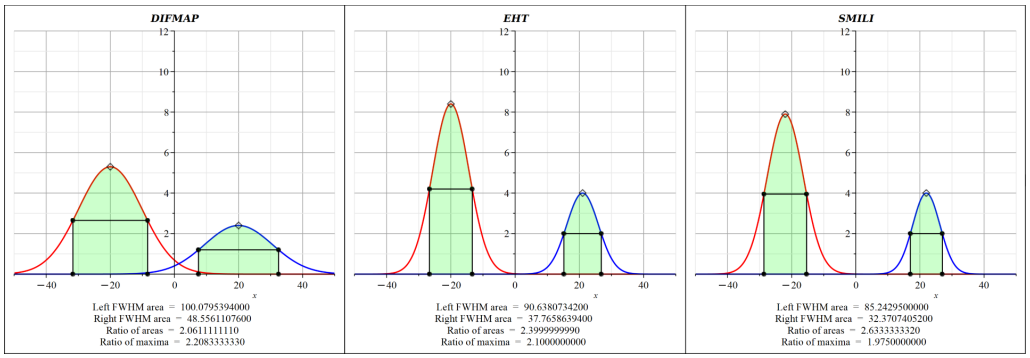


Figure 4.6: *Results of analysis to calculate relative brightness of approaching and receding beams. This is based on measurements from each imaging library in Figure 4.5, by comparing i) the areas under each pair of (Gaussian) curves (to FWHM) and ii) the ratio of maxima. Image credit: Prepared by author.*

Hence

$$2.25 \times (1 - 0.96 \times \frac{V_R}{c})^3 = (1 + 0.96 \times \frac{V_R}{c})^3, \tag{4.6}$$

where $V_R$ is the velocity at radius $R$, located at the inner edge of the accretion disk. Thus, $V_R$ is $\sim$ 0.14c, or $(4.2 \pm 0.3) \times 10^7$ m s$^{-1}$.

## 4.4 The innermost stable circular orbit (ISCO)

Following calculation of the rotation of the accretion disk using the above method, the next step is to estimate the radius of the inner edge of the accretion disk (illustrated in Figure 2.4). As explained in section 4.2, it is assumed that the emission is all arising from the inner accretion disk at the smallest marginal stable orbit, $R_{ISCO}$. Different methods have been used to estimate $R_{ISCO}$ and three different approaches were selected in order to obtain an average value to use in the spin estimate. The methods set out below are by Doeleman et al. (2012), Dokuchaev & Nazarova (2019) and Medeiros et al. (2023).

### 4.4.1 Estimate by Doeleman et al. (2012)

As discussed in Chapter Two, GR provides the mathematical equations that show the dependence of spin on the intrinsic radius of ISCO. However, Doeleman et al. (2012) point out that strong lensing effects, due to the Kerr spacetime metric near the rotating black hole, magnify the apparent size of the ISCO, with the relationship between observed ISCO size and black hole spin set out in Chapter Two (Figure 2.9). Using EHT data at 1.3mm that spatially resolve the base of the jet, Doeleman et al. (2012) calculated a lensed ISCO diameter of 5.5 ± 0.4 Schwarzschild radii ($R_{SCH}$). We convert the estimated ISCO diameter to metres as follows:

1 Schwarzschild radius =

$$2GM/c^2 = (2 \times 6.67 \times 10^{-11} \times 1.3 \times 10^{40})/(3 \times 10^8)^2 = 2 \times 10^{13} m. \tag{4.7}$$

The lensed ISCO radius is thus

$$(0.5) \times (5.5) \times (2 \times 10^{13}) m = 5.5 \times 10^{13} m, \tag{4.8}$$

which is equivalent to ∼22 $\mu as$.

### 4.4.2 Estimate by Dokuchaev & Nazarova (2019)

An alternative approach is used by Dokuchaev & Nazarova (2019), who demonstrate that the observed brightest point in the accretion disk is always placed at $R_{ISCO}$. The EHT images in Figure 4.7 below (which provide a scale in $\mu$as) indicate the brightest point with an 'x'. This was used to manually estimate $R_{ISCO}$ as 21 $\mu as$, a result which aligns with Doeleman's estimate above.

### 4.4.3 Estimate by Medeiros et al. (2023)

A study by Medeiros et al. (2023) used a novel imaging algorithm called PRIMO to reconstruct images of M87*, using the EHT 2017 observational data set. The

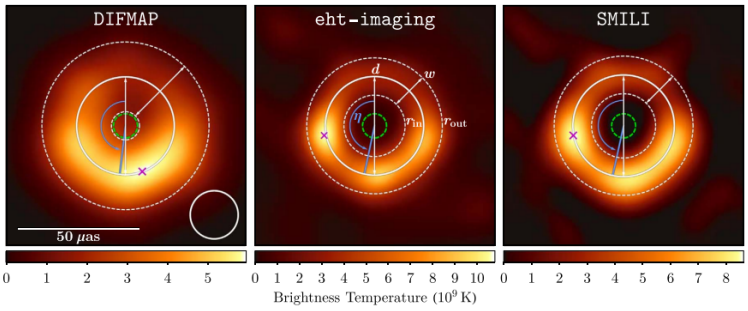


Figure 4.7: *Estimated ring properties overlaid on the April 11 images from each imaging pipeline. The cross in each panel indicates the location of peak ring brightness. Image credit: (EHTC et al., 2019d, Figure 26).*

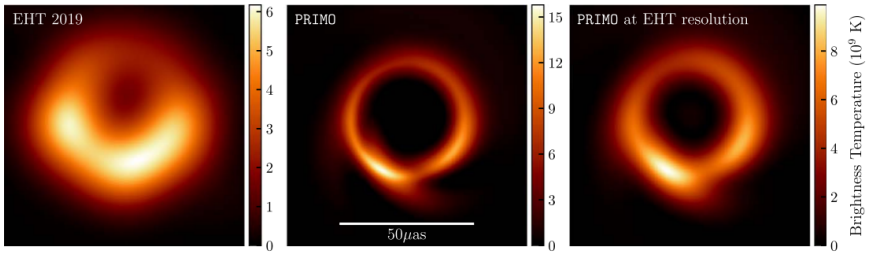


Figure 4.8: *(Left) First EHT image published in (EHTC et al., 2019a). (Middle) Reconstructed image from applying PRIMO to the same data set. (Right) The PRIMO image blurred to the resolution of the EHT array. Image credit: (Medeiros et al., 2023, Figure 1).*

authors argue that the PRIMO image offers a superior use of the resolution of the EHT array. In Figure 4.8, the EHT image (left panel) is compared with the result of generating the image using PRIMO (middle). On the right panel, the PRIMO image has been adjusted to the resolution of the EHT array. Medeiros et al. (2023) suggest that the image morphology in the middle image provides a more accurate estimate of ISCO, compared with the familiar left-hand image originally published by EHT. Using the middle image, the distance from the centre of the ring to the brightest point, located at $R_{ISCO}$, is estimated to be $(15/36) \times 50 = 21$ $\mu$ arcsec. It is interesting to note that this revised value for $R_{ISCO}$ approximates to the difference

between the maximum and minimum brightness (∼20 $\mu$ arcsec) in Figure 4.4, the schematic diagram from EHTC et al. (2019a).

In summary, three different techniques produced consistent estimates for $R_{ISCO}$ of ∼22 $\mu as$, ∼21 $\mu as$ and ∼21 $\mu as$. The average for the value of the inner radius, $R_{ISCO}$, based on the above results, is therefore ∼ 21 ± 2 $\mu as$. Assuming a distance to M87 of 16.8 Mpc, this leads to an estimate for $R_{ISCO}$ of ∼ 5.5 ± 0.5 × $10^{13}$ m.

## 4.5 Spin estimate

The age of M87* is estimated at over 10Gyr and it is assumed that the angular momentum of the inner accretion disk matches the spin of the black hole, which is expected to develop over timescales of ∼ 10Myr (Thorne, 1974). Therefore, we take the product of $V \times R$ per unit mass to be constant from $R_{ISCO}$ down to the black hole event horizon. This gives a value for the black hole angular momentum, $J$, of

$$J \;=\; M_{BH}\, V_R\, R_{ISCO}\,, \tag{4.9}$$

The dimensionless spin parameter, $a$, is defined as

$$a \;=\; \frac{J\,c}{G\,M_{BH}^2}\,, \tag{4.10}$$

where c is the speed of light and G is the gravitational constant. The spin parameter, $a$, is therefore given by

$$a \;=\; \frac{M_{BH}\, V_R R_{ISCO}\, c}{G\,M_{BH}^2} = \frac{V_R\, R_{ISCO}\, c}{G\,M_{BH}} \tag{4.11}$$

As noted in Section 2.3, the mass of M87* has been estimated using different methods, including gas dynamics and stellar kinematics. Given that these results have

been reconciled, we can use the consensus value from EHTC et al. (2019b) of:

$$M_{BH} = (6.5 \pm 0.1) \times 10^9 M_\odot = 1.3 \times 10^{40} \text{ kg}, \tag{4.12}$$

Thus we find

$$a = \frac{(4.2 \times 10^7)(5.5 \times 10^{13})(3 \times 10^8)}{(6.67 \times 10^{-11})(1.3 \times 10^{40})}, \tag{4.13}$$

$$a = 0.8 \pm 0.1\,. \tag{4.14}$$

The author's estimate, based on the new method described above, is a spin parameter, $a \sim 0.8 \pm 0.1$.

## 4.6 Discussion of results

### 4.6.1 Author's spin estimate compared with published studies

In Chapter 2, eight different studies of the M87* spin parameter were outlined. A comparison of the author's estimate with the results of these studies (summarised in Figure 4.9) shows that it is positioned towards the upper end of the range of outcomes, which span from 0.1 to 0.98. As a review of these results has not discerned any obvious pattern, such as a trend over time, it is instructive to consider why there is such a broad range of results.

It is suggested that different methods based on a variety of assumptions are likely to produce divergent results. As spin cannot be measured directly, each method is underpinned by a theoretical argument, that links the spin to one or more measurable parameters. The models reviewed make certain fundamental assumptions e.g. that GR adequately describes the spacetime near the black hole. In addition, each technique is also based on assumptions specific to the model adopted, as illustrated in the case of methods which rely on estimating the location of ISCO. The validity

of key assumptions underlying these techniques is often uncertain. For example, as accretion disc theory is still an active field of research (Reynolds, 2013), assumptions in this area may give rise to a significant source of systematic error in parameter estimates. The author's own spin estimate is no different from these other studies, as it is based on certain key assumptions which are clearly laid out, in order to provide an essential caveat to the reader.

Some studies on M87* spin include an error estimate with their result. For ex-

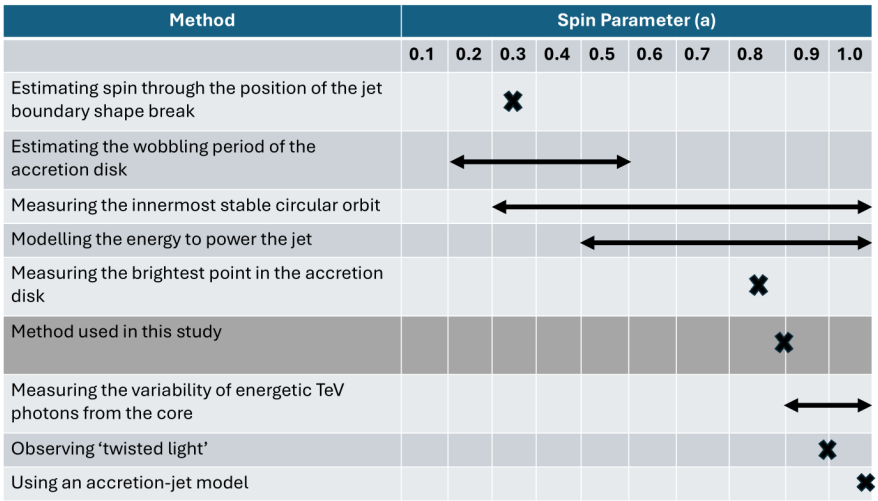


Figure 4.9: *Summary of estimated spin parameter, a, for M87* from eight published studies, based on a range of different methods which were outlined in Chapter 2. Estimates are marked either with an 'x' or a line, if the studies reported a range for the spin parameter. The author's method is highlighted in dark gray. Source: Prepared by author.*

.

ample, Dokuchaev & Nazarova (2019) estimate a value for the spin parameter, a, of 0.75 ±0.15. It is assumed that this error margin is statistical, based on the assumptions set out explicitly in their study. If this is the case, it does not take account of the systematic errors which may arise, due to the limitations of the method used.

It is of note that several other spin estimates reviewed in Chapter 2 have reported results, based on other techniques, which are well outside the published error band of Dokuchaev & Nazarova (2019).

### 4.6.2 Comparing M87* spin with other SMBHs

Earlier studies generally estimated spins across different masses of black hole, rather than focus on particular size categories. For example, Daly (2011) investigated spins in 55 radio-loud sources with jets, although the selected black holes were not restricted to SMBHs. Assuming that the jets are powered (in part or in full) by spin energy, they found an average spin parameter close to a = +0.5, although large uncertainties were reported on individual spin levels.

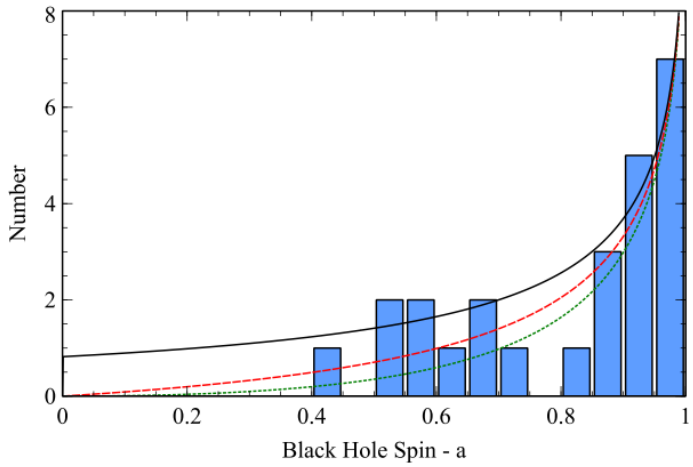


Figure 4.10: *Distribution of spin values, a, for a sample of SMBHs from reflection fitting of x-ray spectra. Source: Vasudevan et al. (2016), Figure 7.*

Recognition of the importance of SMBH spin has been accompanied by an increased research focus on this category of black holes. Most of these studies have been based on x-ray reflection spectroscopy in the Fe K$\alpha$ band (Reynolds, 2013). This technique, which involves locating the position of ISCO, is methodologically biased towards SMBHs with relatively high accretion rates (Reynolds, 2013), which

possess a broad Fe K$\alpha$ line of adequate strength (Brenneman, 2013). The author has not found any results for M87* which use this technique, most likely because it is not viable for low accretion black holes.

Studies by Brenneman (2013) and Vasudevan et al. (2016) have reported spin estimates for $\sim$ 22 SMBHs, based on the x-ray reflection method. There is a strong weighting towards high spins, as over 70 % of the SMBHs have pro-grade spin estimates of a $\geq$ 0.8 (see Figure 4.10). The authors of these studies acknowledge that the relatively small sample gives rise to possible systematic errors, from using the same technique. In addition, there is selection bias arising from the sampling process, with the requirement for a relatively high accretion rate.

One way to assess the reliability of a particular method is to ascertain whether consistent results are obtained from using one or more different techniques. Daly (2019) used the outflow method, based on measuring the beam power of collimated jets, to measure the spin of over 700 SMBHs, obtaining relatively high spin estimates in the range, a = 0.6 to 1. The values for six SMBHs in this study were then compared with estimates from the x-ray reflection method. The results of this comparison, which are set out in Table 1 of Daly (2019), indicate good agreement between these independently determined estimates. A similar close agreement was obtained by Azadi et al. (2023), who extended the work of Daly (2019) and carried out a comparison for an additional 15 SMBHs.

A small number of other SMBH spin studies have been identified in the literature. For example, Ananna et al. (2020) used x-ray surveys to analyse SMBHs and estimate the average efficiency with which their chosen sample convert mass to radiated energy. They conclude that on average these SMBHs are spinning rapidly, with efficiency levels approaching the theoretical limit for a maximally rotating Kerr black hole.

## 4.7 Summary

This Chapter set out the author's estimate of the M87* spin parameter, a $\sim 0.8$, explaining the underlying assumptions on which the method is based. The result is at the upper end of published results for M87*, but aligns with other studies of SMBH spin. Several different techniques have been used by other authors to measure the spin of M87*, which creates model dependency and gives rise to systematic risks. As in the case of the author's estimate, each model has its inherent limitations and uncertainties, diluting the effectiveness of comparing results. Results from most SMBH spin measurements undertaken to-date convey relatively high spin parameters, with $a > 0.6$, in concordance with the author's estimate. Although many studies have been based on x-ray reflection spectroscopy, this is not a suitable option for M87*, given its relatively low accretion rate. The next Chapter discusses the author's estimates of other key M87 parameters, including the accretion rate onto the black hole.

# Chapter 5

# Estimating M87* accretion rate and jet power

## 5.1 Introduction

Following measurement of the angular rotation rate, $V_R$, the radius of the inner edge of the accretion disk, $R_{ISCO}$, and the spin parameter, a, this Chapter sets out an estimate of the M87* accretion rate. This is an important parameter, as the rate of accretion provides insights into the energetics of the black hole system. Although many aspects remain unresolved, it is understood that matter accreting from the interstellar medium powers the jet outflow. The estimate of the M87* accretion rate leads to constraining the kinetic energy per unit time of the accreting material, enabling the power of the accretion to be compared with estimates of the jet power. Estimates of both the accretion rate and accretion energy are compared with published studies and the possible impact of accretion on the evolution of M87* is discussed.

## 5.2 Methods and Results

In this Chapter, the author measures the accretion rate and accretion energy of the black hole M87*. The method used to estimate the accretion rate, $\dot{M}$, involves calculating the accretion velocity and then using the value of $R_{ISCO}$ from Chapter 4, together with assumptions on plasma density and an accretion disk model. These steps are explained below.

### 5.2.1 Estimating the accretion velocity

The first step is to estimate the accretion velocity, which is the component of plasma velocity approaching the black hole. The accretion occurs through the accretion disk, and the accreting matter is expected to be highly ionised. Assuming that the matter is tied to the magnetic field in the disk, data from the polarisation study of M87* (EHTC et al., 2021a) are used to estimate the angle of the accretion flow and thus the component of plasma velocity heading towards the black hole.

It is assumed that the matter tracks the magnetic field and spirals inward in the disk. The angle of the accretion flow, $\alpha$, is obtained from polarised images of M87*, which provide information about the direction of magnetic field lines near its event horizon (EHTC et al., 2021a). As these images convey that the magnetic field in the disk is neither radial nor tangential (EHTC et al., 2021a), we assume that, at each point, it lies at an angle, $\alpha$, to the tangent vector at that point. We also assume that this matter has a total velocity, $V_T$, which is a combination of two components, the rotational velocity, $V_R$, and the accretion velocity, $V_A$.

In order to estimate the angle of the plasma flow, measurements were made using images published by EHTC et al. (2021a) - see their Figure 7. The images and the author's superimposed manual exercise are shown in Figure 5.1. Initially, the position of the centre of the black hole shadow was estimated and then concentric circles drawn. At selected points where these crossed polarisation vectors, the angle

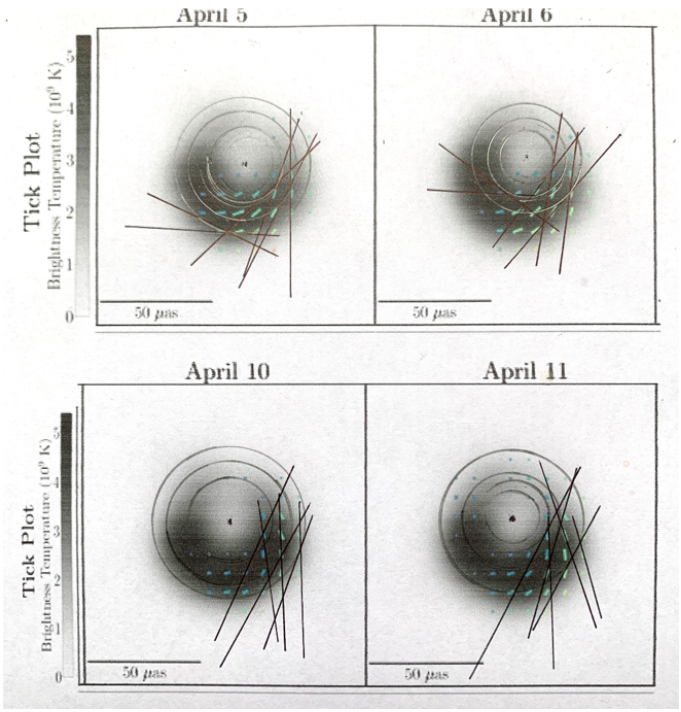


Figure 5.1: *Polarimetric images of M87*, with "field lines" plotted over an underlying total intensity image, using images published by EHTC et al. (2021a) - see their Figure 7. The ticks show the degree and direction of linear polarisation, with the direction indicating the vector position angle. Each image represents an average of the five fiducial images (one per method) for each of the four observed days in 2017.*

between the tangent to the curve at that point and the vector was estimated. The images in Figure 5.1 show the EHTC results of observations over four days in April, 2017. For each of these days, the author made eleven measurements, which took into account that the polarisation map records the electric vector. As this is orthogonal to the magnetic field direction, an adjustment of 90° is required to obtain the direction of the magnetic field.

The results set out in Table 5.1 record the estimated angle in relation to eleven vectors for each day of observations. The error bar is an estimate of the uncertainty of the manual exercise i.e. how far the measuring instrument could be twisted each

way and be judged by eye as a reasonable estimate of the angle. The average vector measurement for each of the four days was computed and the error on the average then estimated. For example, the average vector measurement for April 5 is 57°, with an error of $4/\sqrt{11} \sim 1.2°$. The overall average angle, $\alpha$, was estimated as 58.5°, which is the average of the measurements from the four days. The error bar on this was obtained by averaging each of the daily average error estimates, giving $1.2/\sqrt{4} = 0.6°$. Overall, the angle $\alpha$ was thus estimated at $(58.5 \pm 0.6)°$.

| Date of Observation | April 5 | April 6 | April 10 | April 11 |
|---|---|---|---|---|
| Vector 1 | 60 ± 4° | 60 ± 4° | 58 ± 4° | 55 ± 4° |
| Vector 2 | 61 ± 4° | 58 ± 4° | 58 ± 4° | 45 ± 4° |
| Vector 3 | 65 ± 4° | 59 ± 4° | 67 ± 4 ° | 60 ± 4° |
| Vector 4 | 59 ± 4° | 56 ± 4° | 56 ± 4° | 52 ± 4° |
| Vector 5 | 64 ± 4° | 60 ± 4° | 61 ± 4° | 53 ± 4° |
| Vector 6 | 66 ± 4° | 61 ± 4° | 62 ± 4° | 48 ± 4° |
| Vector 7 | 27 ± 4° | 59 ± 4° | 48 ± 4° | 51 ± 4° |
| Vector 8 | 45 ± 4° | 44 ± 4° | 64 ± 4° | 49 ± 4° |
| Vector 9 | 68 ± 4° | 54 ± 4° | 72 ± 4° | 61 ± 4° |
| Vector 10 | 46 ± 4° | 51 ± 4° | 51 ± 4° | 56 ± 4° |
| Vector 11 | 66 ± 4° | 58 ± 4° | 59 ± 4° | 55 ± 4° |
| Average | 57 ± 1° | 58 ± 1° | 62 ± 1° | 57 ± 1° |

*Table 5.1. Results of manual exercise to estimate the angle between polarisation vectors and the tangent to the orbital curve (see Figure 5.1), adjusted by 90° to obtain the direction of the magnetic field. The overall average angle over the four days is (58.5 ± 0.6)°. Prepared by author.*

Given the relationship between total velocity, $V_T$, rotational velocity, $V_R$, and the accretion velocity, $V_A$, elementary geometry shows us that $V_A = V_R \tan \alpha$. Hence

$V_A$, the component of the plasma velocity heading towards the black hole, is

$$V_R \times \tan 58.5^\circ = (4.2 \times 10^7) \times 1.63 \sim 7 \times 10^7 ms^{-1}. \quad (5.1)$$

The error-bar on $V_A$ is estimated by considering the errors on $V_R$ and $\tan \alpha$. The error bar on $V_R$ is estimated at $\sim 7\%$ (see Chapter 4). Taking into account the error bar on $\alpha$, the lower and upper values are:

$$\tan(58.5 - 0.6)^\circ = \tan 57.9^\circ = 1.59 \quad (5.2)$$

$$\tan(58.5 + 0.6)^\circ = \tan 59.1^\circ = 1.67 \quad (5.3)$$

We thus obtain tan (58.5 +/- 0.6)° = 1.63 +/- 0.04. Given that 0.04/1.63 = 2.5%, we estimate the error on $\tan \alpha$ as $\sim$ 2.5%. The error bar on $V_A$ is thus roughly $\pm \sim 10\%$, giving a value for the accretion velocity of $V_A = (7 \pm 0.7) \times 10^7$ ms$^{-1}$ or $(0.23 \pm 0.02)$c. The error introduced by considering the tilt to the plane of the sky is small (see Section 4.3).

### 5.2.2 Plasma density

The next step in calculating the accretion rate is to estimate the plasma density, which is discussed in EHTC et al. (2021b). This gives a range for the emission region plasma density as equivalent to $n(e)$ being $\sim 10^4 - 10^7$ cm$^{-3}$ (EHTC et al., 2021b). Assuming the gas is completely ionised and ignoring the mass of the electrons and helium, the density, $\rho$, can therefore be approximated as lying between 1.7 $\times 10^{-17}$ kg m$^{-3}$ and 1.7 $\times 10^{-14}$ kg m$^{-3}$. This range conveys the considerable level of uncertainty in plasma density.

### 5.2.3 Accretion model

Let us assume that the accretion takes place from part of an imaginary sphere around the black hole of radius $R_{ISCO}$ (see schematic diagram in Figure 5.2). Matter is

approaching the event horizon from $R_{ISCO}$ at $V_A$, meaning that a layer $V_A$ thick passes the inner edge of $R_{ISCO}$ every second. Although we have estimates for $V_A$ and $\rho$ for the inwardly moving plasma at $R_{ISCO}$, we need to consider what further assumptions are necessary to complete our calculation of the accretion rate.

We assume that accretion is from an accretion disk, which represents only a fraction of the total area of the imaginary sphere either side of the equatorial plane of the disk. In order to simplify the approach, we consider two scenarios i.e. accretion from i) a thick disk and ii) a thin disk. In the first case, we assume that the angle subtended by the inner edge of the disk to be a maximum of $\sim \pm 30^\circ$ above and below the mid-plane of the disk, or $\sim 1$ radian in total. In the second scenario, we assume that the angle subtended by the inner edge of the disk to be a maximum of $\sim \pm 3^\circ$ above and below the mid-plane of the disk, or $\sim 0.1$ radians in total.

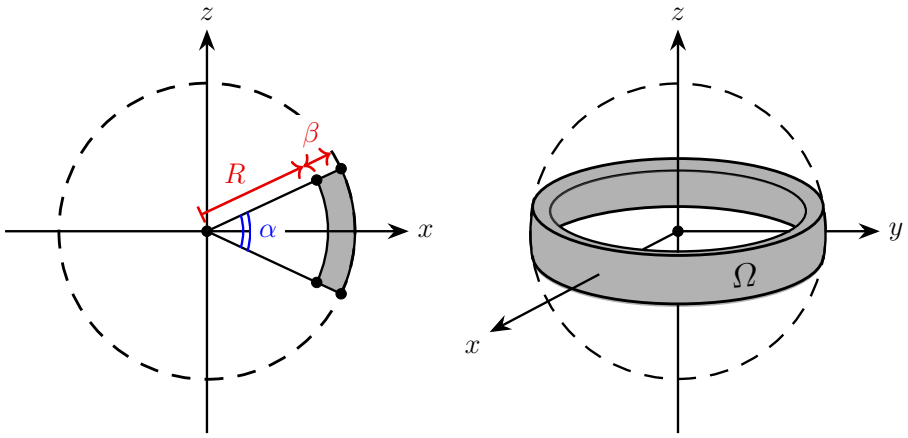


Figure 5.2: *A schematic diagram illustrating the accretion disk model used in estimating the accretion rate. The shaded sector (left) is rotated around the z-axis (right). Source: Paper by Drew et al. (2024), currently under peer-review.*

We use spherical polar coordinates ($r$, $\theta$ and $\phi$), over suitable limits. We consider an annular sector of radius R and thickness $\beta$, subtending an angle $\alpha$ at the centre, as illustrated in Figure 5.2 (left). We model the accreting mass as an annular section rotated around the z-axis, as shown in Figure 5.2 (right).

The infinitesimal volume element of the region $\Omega$ is:

$$dV = r^2(\sin\theta)\, dr\, d\theta\, d\phi \tag{5.4}$$

We integrate from r=R to r=R $+\beta$ (with respect to coordinate r), from $(\pi-\alpha)/2$ to $(\pi+\alpha)/2$ (with respect to $\theta$) and from 0 to $2\pi$ (with respect to coordinate $\phi$). The volume integral is thus

$$\int\int\int_{\Omega} dV = \int_{r=R}^{r=R+\beta}\int_{\theta=(\pi-\alpha)/2}^{\theta=(\pi+\alpha)/2}\int_{\phi=0}^{\phi=2\pi} r^2\sin\theta\, dr\, d\theta\, d\phi \tag{5.5}$$

$$= \left[\frac{r^3}{3}\right]_{r=R}^{r=R+\beta} \times [-\cos\theta]_{\theta=(\pi-\alpha)/2}^{\theta=(\pi+\alpha)/2} \times 2\pi \tag{5.6}$$

$$= \frac{1}{3}[(R+\beta)^3 - R^3] \times [-\cos(\frac{\pi+\alpha}{2}) + \cos(\frac{\pi-\alpha}{2})] \times 2\pi \tag{5.7}$$

$$= \frac{2\pi}{3}[(R^3 + 3R^2\beta + 3R\beta^2 + \beta^3) - R^3] \times [\sin(\frac{\alpha}{2}) + \sin(\frac{\alpha}{2})] \tag{5.8}$$

$$= \frac{4\pi}{3}[(3R^2\beta + 3R\beta^2 + \beta^3) - R^3] \times [\sin(\frac{\alpha}{2})] \tag{5.9}$$

$$= 4\pi R^2[\beta + \frac{\beta^2}{R} + \frac{\beta^3}{3R^2}]\sin(\frac{\alpha}{2}). \tag{5.10}$$

The mass of the accreting matter is given by:

$$M = \rho\, Vol[\Omega] = 4\pi\,\rho\, V_A\, R^2 \left(t + \frac{V_A\, t^2}{R} + \frac{V_A^2\, t^3}{3R^2}\right)\sin\left(\frac{\alpha}{2}\right) \tag{5.11}$$

where $\rho$ is the mass density and $\beta$ is the the thickness of the accreting matter i.e. the accretion velocity $V_A$, multiplied by the accretion time $t$ ($\beta = V_A t$). Assuming a steady-state accretion, the accretion rate is then:

$$\dot{M} \;=\; \frac{dM}{dt} \;=\; 4\pi\,\rho\, V_A\, R_{ISCO}^2 \left(1 + \frac{V_A\, t}{R_{ISCO}}\right)^2 \sin\left(\frac{\alpha}{2}\right). \tag{5.12}$$

We assume the inner radius $R$ is much larger than the thickness of the accreting matter: $R_{ISCO} \gg \beta = V_A t$, implying $V_A\, t/R_{ISCO} \ll 1$ and hence

$$\dot{M} \;=\; 4\pi\, \rho\, V_A\, R_{ISCO}^2 \sin\left(\frac{\alpha}{2}\right). \tag{5.13}$$

Our estimate of the accretion rate is based on the thick and thin disk approximations, together with the values of $V_A$, $R_{ISCO}$ and $\alpha$ obtained from the methods explained above and the range of values for $\rho$ from the EHTC. We now consider accretion rate approximations for the two specific cases outlined above i.e. accretion from i) a thick disk and ii) a thin disk, as follows:

i) Thick disk model, upper density limit

Assuming a thick disk with $\alpha = 60°$, $\alpha = \pi/3$ radians and $\sin(\alpha/2) = \sin\,(\pi/6) = 1/2$.

The accretion rate is thus

$$\dot{M} \;=\; 2\pi\, \rho\, V_A R_{ISCO}^2. \tag{5.14}$$

$$\dot{M} = 2\pi \times\, (1.7 \times 10^{-14})(7 \times 10^{7})\,(5.5 \times 10^{13})^2, \tag{5.15}$$

$$\dot{M} = 2.3 \times 10^{22} kgs^{-1} \tag{5.16}$$

The error on this is estimated at roughly $\pm \sim 28\%$, based on $\pm \sim 10\%$ for $V_A$ and $\pm \sim 9\%$ for $R_{ISCO}$ (see Chapter 4). Thus

$$\dot{M} = (2.3 \pm 0.6) \times 10^{22} kgs^{-1} \tag{5.17}$$

We can convert to $M_\odot$ per annum, giving:

$$\dot{M} = \frac{(2.3 \times 10^{22}) \times\, (3.15 \times 10^{7})}{2 \times 10^{30}} \sim (4 \pm 1) \times 10^{-1}\, M_\odot\, yr^{-1}. \tag{5.18}$$

Based on these assumptions, the accretion rate is $\sim (2.3{\pm}0.6){\times}10^{22}\,\mathrm{kgs}^{-1}$ or $(4{\pm}1)$ ${\times}10^{-1}\ M_\odot \mathrm{yr}^{-1}$

ii) Thick disk model, lower density limit

This calculation is similar to i) above, but assumes that the density, $\rho$, is 1.7 $\times$ $10^{-17}$ kg m$^{-3}$. The accretion rate is thus

$$\dot{M} = 2\pi \times (1.7 \times 10^{-17})(7 \times 10^{7})\,(5.5 \times 10^{13})^{2}, \tag{5.19}$$

$$= (2.3 \pm 0.6) \times 10^{19} kgs^{-1} \tag{5.20}$$

We can convert to $M_{\odot}$ per annum, giving:

$$\dot{M} = (4 \pm 1) \times 10^{-4} M_{\odot}\ yr^{-1}. \tag{5.21}$$

Based on these assumptions, the accretion rate is $\sim$ (2.3$\pm$0.6)$\times 10^{19}$ kgs$^{-1}$ or (4$\pm$1) $\times 10^{-4}$ $M_{\odot}$yr$^{-1}$

iii) Thin disk model, upper density limit

In this scenario, we assume a thin disk with $\alpha = 6^{\circ}$, $\alpha = \pi/30$ radians and sin($\alpha$/2) = sin ($\pi$/60) = $\sim$ 0.05. The accretion rate is thus

$$\dot{M} = (\pi^{2}/15)\,\rho\, V_{A} R_{ISCO}^{2}. \tag{5.22}$$

$$\dot{M} = \frac{\pi^{2} \times (1.7 \times 10^{-14})(7 \times 10^{7})\,(5.5 \times 10^{13})^{2})}{15}, \tag{5.23}$$

$$= (2.4 \pm 0.7) \times 10^{21} kgs^{-1} \tag{5.24}$$

Converting to $M_{\odot}$ per annum, the accretion rate

$$\dot{M} = (4 \pm 1) \times 10^{-2} M_{\odot} yr^{-1} \tag{5.25}$$

Based on these assumptions, the accretion rate is $\sim$ (2.4$\pm$0.7)$\times 10^{21}$ kgs$^{-1}$ or (4$\pm$1) $\times 10^{-2}$ $M_{\odot}$yr$^{-1}$

iv) Thin disk, lower density limit

This calculation is similar to iii) above, but assumes that the density, $\rho$, is 1.7 $\times$ $10^{-17}$ kg m$^{-3}$. The accretion rate is thus

$$\dot{M} = (\pi^{2}/15)\,\rho\, V_{A} R_{ISCO}^{2}. \tag{5.26}$$

$$\dot{M} = \frac{\pi^2 \times (1.7 \times 10^{-17})(7 \times 10^7)(5.5 \times 10^{13})^2)}{15}, \tag{5.27}$$

$$= (2.4 \pm 0.7) \times 10^{18} kgs^{-1} \tag{5.28}$$

We can convert to $M_\odot$ per annum, giving:

$$\dot{M} = (4 \pm 1) \times 10^{-5} M_\odot \ yr^{-1}. \tag{5.29}$$

Based on these assumptions, the accretion rate is $\sim (2.4\pm0.7)\times10^{18}\,\mathrm{kgs}^{-1}$ or $(4\pm1)\times10^{-5}\ M_\odot\mathrm{yr}^{-1}$

In summary, the above calculations show that, in general, accretion from the thick disk model is ten times higher than for the thin disk. If we take into account the three orders of magnitude between the density predictions of the EHTC, the author's accretion rate estimate is in the range $\sim (4\pm1)\times10^{-5}$ and $(4\ \pm1)\times\ 10^{-1}$ $M_\odot$ yr$^{-1}$. The summary in Table 5.2 shows that the highest accretion rate is in a thick disk at the upper density limit, while the lowest accretion level is in a thin disk at the lower density limit.

| | Upper Density Limit | Lower Density Limit |
|---|---|---|
| Thick disk | $(2.3\pm0.6)\times10^{22}\,\mathrm{kgs}^{-1}$ or $(4\pm1)\ \times10^{-1}M_\odot\ yr^{-1}$ | $(2.3\pm0.6)\times10^{19}\,\mathrm{kgs}^{-1}$ or $(4\pm1)\ \times10^{-4}M_\odot\ yr^{-1}$ |
| Thin disk | $(2.4\pm0.7)\times10^{21}\,\mathrm{kgs}^{-1}$ or $(4\pm1)\ \times10^{-2}M_\odot\ yr^{-1}$ | $(2.4\pm0.7)\times10^{18}\,\mathrm{kgs}^{-1}$ or $(4\pm1)\ \times10^{-5}M_\odot\ yr^{-1}$ |

*Table 5.2. Accretion rate estimates (including error bars) for thick/thin disk scenarios, assuming upper and lower density limits from EHTC et al. (2021b).*

## 5.3 Accretion energy

The kinetic energy per unit time of the accreting material is calculated by multiplying half the estimated accretion rate by $V_A^2 = (0.23c)^2$. The minimum value of

accretion energy per unit time ('thin' disk, minimum $\rho$), is $6 \times 10^{33}$ $\mathrm{Js}^{-1}$, or of the order of $\sim 10^{34}$ $\mathrm{Js}^{-1}$. The maximum value of accretion energy per unit time ('thick' disk, maximum $\rho$), is $6 \times 10^{37}$ $\mathrm{Js}^{-1}$, or of the order of $\sim 10^{38}$ $\mathrm{Js}^{-1}$.

| | Upper Density Limit | Lower Density Limit |
|---|---|---|
| Thick disk | $(6\pm3)\times10^{37}\,\mathrm{Js}^{-1}$ | $(6\pm3)\times10^{34}\,\mathrm{Js}^{-1}$ |
| Thin disk | $(6\pm3)\times10^{36}\,\mathrm{Js}^{-1}$ | $(6\pm3)\times10^{33}\,\mathrm{Js}^{-1}$ |

*Table 5.3. Accretion power estimates (including error bars) for thick/thin disk and upper/lower density scenarios.*

## 5.4 Discussion of results

### 5.4.1 Accretion rate and implications for development of M87*

The author estimates an accretion rate between $\sim (4 \pm 1) \times 10^{-5}$ and $(4 \pm 1) \times 10^{-1}$ $M_\odot$ $\mathrm{yr}^{-1}$. The rough tracking of error bars illustrates that random errors are significantly smaller than the systematic errors inherent in this exercise. The result is broadly in line with the wide range of estimates published by other studies. For example, research based on Chandra x-ray observations concluded that gas accretes onto M87* at a rate of $0.1 M_\odot$ $\mathrm{yr}^{-1}$ (Di Matteo et al., 2003a). A later study by Kuo et al. (2014), which analysed polarisation data to estimate the Faraday rotation measure associated with the accretion flow, obtained an upper limit of $\sim 10^{-3}$ $\mathrm{M}_\odot$ $\mathrm{yr}^{-1}$, also within our range. Russell et al (2015) estimate the accretion rate at 0.1 to 0.2 $\mathrm{M}_\odot$ $\mathrm{yr}^{-1}$, although they indicate it could be two orders of magnitude lower. A further study, based on 2017 EHT observations, estimates the accretion rate at $\sim 10^{-3}$ $\mathrm{M}_\odot$ $\mathrm{yr}^{-1}$ (Lu et al., 2023). This is consistent with the analysis of the flux density in the M87* image by EHTC et al. (2019e), which produced a similar

estimate.

Several studies e.g.:- Reynolds et al. (1996) and Di Matteo et al. (2003b) investigate the level of accretion onto M87*. They find that it has a relatively low rate, which is accompanied by a significantly lower central source emission from the M87 nucleus than would be predicted, based on a standard radiative efficiency. These results have implications for the possible evolutionary path of M87*. As discussed in Chapter 1, this is an important topic as it is likely that massive galaxies, such as M87, co-evolve with their central black holes (Graham, 2023). In principle, a black hole having a mass similar to M87*, $\sim 6 \times 10^9\ M_\odot$, could be accreted at 0.5 solar masses per year over 12 billion years (rough age of the universe). This raises the question as to how M87* developed, if it accretes at the author's estimated rate of between $\sim 4 \times 10^{-5}$ and $4 \times 10^{-1}\ M_\odot\ \mathrm{yr}^{-1}$, which aligns with other studies.

Various explanations have been put forward. It is possible that the original mass of M87* was very large and the black hole formed early in the universe, perhaps when the last merger created the M87 galaxy (Garofalo, 2020). In order to explain the build up in mass, Garofalo (2020) has suggested that M87* was originally accreting at a much higher level than at present and transitioned to a very low accretion rate over billions of years. Another theory is that the central engine of M87 undergoes on-off activity cycles, although the mechanism for this is unclear (Owen et al., 2000). It is also likely that jet flows have a role in influencing the accretion through feedback mechanisms. For example, Di Matteo et al. (2003b) provide a calculation demonstrating that the energy dissipated into the ISM by the jet may reduce the accretion rate, sufficiently to explain its low core luminosity.

It is instructive to consider research findings from investigation of accretion flows in SgrA*, given its low accretion rate and emission levels (EHTC et al., 2022b). As explained in Chapter 1, the EHTC has used both M87* and Sgr A* as laboratories in which the processes that lead to accretion and ejection flows in the core of galaxies

can be researched. While there is no clear signature of an outflow from SgrA*, theorists have suggested structures that may impact on its accretion level and explain emission levels (Ressler et al., 2023). For example, one study finds evidence for an outflowing nuclear wind preventing material falling into the SgrA* accretion disk and quenching accretion (Royster et al., 2019). Another suggests that outflows interact with their surroundings and form a cavity inside the flow, impeding accretion onto SgrA* (Wang et al., 2023). This focus of research activity complements the study of M87* and may provide possible explanations relevant to M87* and other SMBHs.

Research on this topic remains at an early stage, given that the range of events that may have influenced the development of M87* are not well understood. At this juncture, it is not possible to discern its evolutionary path with any confidence.

### 5.4.2 Accretion power and jet power

The author's estimate of the accretion energy per unit time is in the range $\sim 10^{34}$ $\mathrm{Js}^{-1}$ to $\sim 10^{38}$ $\mathrm{Js}^{-1}$. This compares with an accretion power of $5 \times 10^{37}$ $\mathrm{Js}^{-1}$ reported by Di Matteo et al. (2003b) and an estimate in the range $5 \times 10^{37}$ $\mathrm{Js}^{-1}$ to $10^{38}$ $\mathrm{Js}^{-1}$ by Russell et al. (2015).

Although there is currently no consensus on the physical mechanisms that drive the jet in M87* and other similar SMBHs, a range of models has been put forward by way of explanation (Meier, 2012). Two of the main models, developed by Blandford & Znajek (1977) and Blandford & Payne (1982), were outlined in Chapter 2. These studies investigate the energy that powers the black hole 'engine', including the energy of accreting matter and the impact of black hole rotation on magnetic field lines, which permeate the accretion disk. Some authors have also suggested a hybrid model, which combines these processes e.g.: Meier (1999) and Hawley & Krolik (2006).

Given that the author has estimated the accretion power of M87*, it is instructive to compare this result with the power of its jet. There have been several estimates of M87's jet power, typically ranging from $10^{34}$ to $10^{37}$ J$s^{-1}$ (see Table 5.4). This

| Jet power (J$s^{-1}$) | Reference |
|---|---|
| $\sim 10^{37}$ | Bicknell & Begelman (1996) |
| $2 \times 10^{36}$ | Reynolds et al. (1996) |
| $3 \times 10^{35}$ | Young et al. (2002) |
| $\sim 10^{37}$ | Stawarz et al. (2006) |
| $5 \times 10^{36}$ | Bromberg & Levinson (2009) |
| $4 \times 10^{34}$ | Prieto et al. (2016) |

*Table 5.4. Estimates of M87* jet power from published studies.*

wide range reflects the different assumptions and models used in these studies (Broderick et al., 2015). The methodologies used are often based on observations over different lengths and timescales and thus depend on the recent history of M87* activity. If data is sampled over a different epoch, it may not provide useful information on the prevailing state of the M87* engine during the EHTC 2017 observation period, from which data has been analysed in this work. Given this uncertainty, the EHTC has adopted a lower limit of $10^{35}$ J$s^{-1}$ for the M87* jet power, which they regard as conservative (EHTC et al., 2019e).

It can be seen that the author's estimate of M87* accretion power aligns with published estimates for its jet power. The fact that the range of values obtained is consistent with the estimated power of the jet, means that these results support models where it is the power of the accretion that powers the jet.

## 5.5 Summary

This Chapter set out the author's calculation of the M87* accretion rate, estimated to be between $\sim 4 \times 10^{-5}$ and $4 \times 10^{-1}$ $M_{\odot}$ yr$^{-1}$. This wide range reflects considerable uncertainty about the plasma density and different assumptions about the disk model. Accretion is the primary power source behind M87* and accretion power is estimated in the range from $\sim 10^{34}$ J/s (for a 'thin disk') to $\sim 10^{38}$ J/s (for a 'thick' disk). As this range is similar to published estimates of jet power, the author's result favours models which suggest that accretion flow powers the jet.

The author's estimates of the M87* accretion rate and jet power are consistent with published values from other studies. Consideration was given to the impact of the current low accretion level on the evolution of M87*. Explanations include the likely variability of accretion over billions of years, with possible cycles of activity, and the influence of the powerful jet on the accretion process. The next Chapter provides an overview of the research project, together with the limitations of the study and future work to progress M87* research.

# Chapter 6

# Summary and Future Work

## 6.1 Overview of the research project

This study has investigated the black hole in M87, focusing on recent observational research by the EHTC. The strong progress of this programme has produced valuable data, generating significant research output. This is evidenced by over 200 papers created by the EHTC since 2020 which, along with other research, provide a rich source of study material.

In this thesis, the fundamental characteristics of black holes were described and the elements of the M87* system explained. The most important characteristics are mass, which is well constrained, and spin. Understanding the spin of M87* is as important as understanding how it grows in mass (Berti & Volonteri, 2008). Following an outline of different approaches to measuring the M87* spin, a review of eight studies illustrated the wide range of spin estimates obtained from using a variety of techniques. The EHTC initiative was discussed, including the technique of VLBI, which has been successfully exploited to produce the first images of M87*. This breakthrough followed refinement of the EHT array and enhancements in data processing, imaging and analysis techniques.

CHAPTER 6

The EHTC followed its success in producing M87* images from the 2017 observational programme, investigating the polarisation of the ring and the magnetic field structure near the event horizon. Following further improvements to the EHT array, the EHTC published results from its 2018 observational programme, confirming the consistency of the black hole shadow's size and shape. However, during a period of one year the bright region shrank slightly in extent, although the author's analysis shows that the brightest spot remained static.

In this study, obervational data from the EHTC were used to estimate the following key M87* parameters, using basic physics and a simplified mathematical approach.

| M87* Parameter | Author's Estimate | Published Value(s) |
|---|---|---|
| Mass | $(6.4 \pm 0.6) \times 10^9 M_\odot$ | $6.5 \pm 0.2(\text{stat}) \pm 0.7(\text{sys}) \times 10^9 M_\odot$ |
| Rotational velocity | $(4.2 \pm 0.3) \times 10^7$ m s$^{-1}$ or $(0.14 \pm 0.01)$c | N/A |
| Spin parameter, a | $0.8 \pm 0.1$. | 0.1 to 0.98 |
| Accretion velocity | $(7 \pm 0.7) \times 10^7$ m s$^{-1}$ or $(0.23 \pm 0.02)$c. | N/A |
| Accretion rate (range) | $(4 \pm 1) \times 10^{-5}$ and $(4 \pm 1) \times 10^{-1} M_\odot \text{yr}^{-1}$ | $10^{-3}$ and $10^{-1} M_\odot \text{yr}^{-1}$ |
| Accretion power/Jet power (range) | Accretion power $\sim 10^{34}$ to $10^{38}$ J/s | Jet power $\sim 10^{35}$ to $10^{38}$ J/s |

Table 6.1. Parameters estimated in this study v. published values (where available)

Mass and angular momentum represent the two key properties that describe a black hole (Kerr, 1963). This study puts forward a proposed new method to estimate the M87* spin, based on several important assumptions. The result is a spin parameter of $a \sim 0.8$, which is towards the higher end of published estimates,

which span the range $\sim 0.1$ to 0.98. Published results of spin estimates for other SMBHs suggest that most have relatively high spins, with spin parameter a $\geq 0.6$, in concordance with the author's estimate.

Apart from estimating these key characteristics, it is important to investigate other M87* parameters to improve our overall understanding of the black hole. The author's estimate for the mass accretion rate is between $\sim 4 \times 10^{-5}$ and $4 \times 10^{-1}$ $M_{\odot}$ yr$^{-1}$, a wide range that reflects several key uncertainties. This range is consistent with other published estimates, including EHTC et al. (2021b). Two of the largest uncertainties relate to the plasma density (given a difference of three orders of magnitude between EHTC's upper and lower estimate) and assumptions made regarding the disk model (e.g. thin or thick). The minimum value of accretion energy per unit time (based on 'thin' disk assumptions and relatively low $\rho$), is of the order of $\sim 10^{34}$ J/s, while the maximum value ('thick' disk and relatively high $\rho$), is $\sim 10^{38}$ J/s. The power of the jet has previously been estimated to be in a similar range (EHTC et al., 2019e). The author's range of values is thus consistent with the estimated jet power, which means that our result aligns with models where the power of the accretion powers the jet.

In summary, the author has combined EHT imaging and polarimetry data from M87* to make new estimates of the rotation of the disk, the spin of the black hole, the accretion through the disk, the accretion rate onto the black hole and the kinetic energy of the accreting material. The values obtained are consistent with previous published estimates, where available.

## 6.2 Limitations of study

Black hole physics probes the frontiers of knowledge in extreme conditions, often seeming to pose intractable problems for researchers. Whilst great progress has been made in M87* research, acquiring accurate and reliable observational data to test

theoretical models and simulation results remains elusive. This study has illustrated that there is currently no consensus on the spin of M87*, which would enable us to completely characterise the intrinsic properties of the black hole. Measuring spin has been described as a research topic still in its infancy (Brenneman, 2013) and one of the grand challenges of astrophysics (Kawashima et al., 2019). This was conveyed in Chapter 2 by the wide span for the estimated dimensionless spin parameter, from 0.1 to 0.98. As a further illustration of current observational constraints, the EHT Collaboration has not, as yet, ventured its own spin estimate from imaging the black hole shadow, pointing out that the data obtained are currently not sufficiently accurate (EHTC et al., 2019f). The increase in research output on this topic will, over time, help to develop more robust methods to measure spin, noting the span of fifty years from Luminet's simulated photo of a black hole (see Figure 1.2) until the first image of M87* was published.

In order to estimate key parameters, it was necessary to make a range of assumptions, which have been set out in the relevant Chapters. This was partly to simplify calculations, but also reflected limitations in published data on some parameters (e.g. plasma density). Further observational progress is needed in order to refine the models used, enabling similar results from different approaches. By overcoming these technical limitations, more precise data from close to the core will result in consistent and reproducible outcomes from analysis of measurements obtained.

## 6.3 Future work to progress M87* research

Given that improving our understanding of M87* tests the frontiers of research capabilities, it is essential that momentum be maintained to ensure continued advances in all aspects of this research. Inferring the key parameters of M87* is currently limited not only by observational shortcomings, but also in large part by theoretical uncertainties (Ricarte et al., 2023). For example, further progress in measuring the

spin of M87* and other SMBHs will rely on the development of improved methodologies, together with enhanced observational capabilities. Simulation studies will also remain an important aspect of this research. Specifically in relation to the author's study, it is suggested that testing the methods and results set out in this thesis, using GRMHD simulations, would be a worthwhile exercise.

Following the successful 2017 observational programme, enhancements were made to the EHT array, which produced improvements in the 2018 results. The Greenland telescope was added which, in particular, improved the coverage of the array in the North-South direction. The Large Millimeter Telescope, the world´s largest single-dish steerable millimetre-wavelength telescope (Hughes et al., 2010), also contributed its 50m surface for the first time. In addition, the array was enhanced to carry out observations in four frequency bands around 230 GHz (two more bands than in 2017). Raymond et al. (2024) recently reported the first VLBI observations at 870$\mu$m wavelength (345 GHz frequency). Operation at this short wavelength, with planned EHT enhancements, will result in further improvements of angular resolution to better than 20 $\mu$as. Although decreasing the VLBI wavelength presents technical challenges, it enhances the capability of the EHT to probe the dynamics near the event horizon.

Building on this success, the next generation Event Horizon Telescope (ngEHT) will be a significant enhancement to the existing telescope. The geographical footprint of the array will be expanded, with approximately 10 new dishes, and observations are planned at three frequencies simultaneously (Roelofs et al., 2023). These significant additional observational capabilities will be complemented by continuing technical advances in several areas. As an illustration of this progress, Doeleman et al. (2023) note that, over the last twenty years, the bandwidth of VLBI systems has corresponded with Moore's Law - a doubling of capacity and speed approximately every 18 months (see Figure 6.1). Together, these enhancements will provide

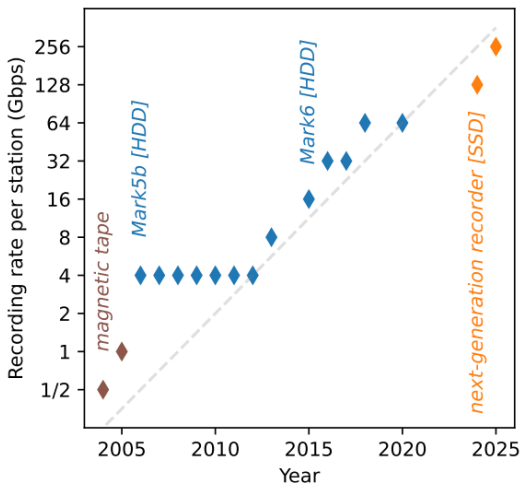


Figure 6.1: *Illustrates recent technical advances in data capture. Since the early 2000's, the recording rate for EHT stations has nearly doubled every two years. Maintaining this pace of development in data capture has required continual upgrades, using the latest commercial technologies. Source: Doeleman et al. (2023), Figure 1.*

better ($u$,$v$) coverage, increased sensitivity, and frequency coverage (Roelofs et al., 2023).

Improved quality images and videos will help ngEHT to deliver its key science goals. These include more accurate measurement of black hole shadows, measuring SMBH spin, investigating the evolutionary paths of SMBHs and probing the mechanisms that drive accretion (Doeleman et al., 2023). The initiative will seek to extend its investigations beyond M87* and Sgr*, targeting several dozen SMBHs with its horizon-scale resolution, in order to measure their mass and spin (Pesce et al., 2022).

## 6.4 Concluding remarks

Progress in the investigation of SMBHs, in particular M87*, has made strides in recent years. M87* was the first black hole to be imaged (EHTC et al., 2019a) and has been described as the best studied jet/accretion flow/black hole system (Anantua et al., 2024). This has generated significant research findings, evidenced by over 200 papers created by the EHTC since 2020, which provide a rich source of study material. The output reflects the importance of M87* as a research topic, with recent observational progress by the EHTC motivating the author's project. This study has focused on estimating key parameters of M87*, using a simplified mathematical approach. It uses observational findings from the EHTC to consider the mass of M87*, carry out a null hypothesis test of GR and develop new estimates for the spin and accretion rate of M87*. The results are consistent with the values obtained by other published studies. In order to achieve new and exciting science, the EHTC plans to further improve its existing array and develop the ngEHT. Undoubtedly, these initiatives will provide significant new insights to improve understanding of the complex astrophysics of M87* and other SMBHs.

# Bibliography


Ananna T. T., et al., 2020, http://dx.doi.org/10.3847/1538-4357/abb815 , https://ui.adsabs.harvard.edu/abs/2020ApJ...903...85A 903, 85

Anantua R., et al., 2024, http://dx.doi.org/10.1093/mnras/stad3998 , https://ui.adsabs.harvard.edu/abs/2024MNRAS.528..735A 528, 735

Asada K., Nakamura M., 2012, http://dx.doi.org/10.1088/2041-8205/745/2/L28 , https://ui.adsabs.harvard.edu/abs/2012ApJ...745L..28A 745, L28

Azadi M., et al., 2023, http://dx.doi.org/10.3847/1538-4357/acbe9c , https://ui.adsabs.harvard.edu/abs/2023ApJ...945..145A 945, 145

Bambi C., Freese K., 2009, http://dx.doi.org/10.1103/PhysRevD.79.043002 Phys. Rev. D, 79, 043002

Bambi C., et al., 2021, http://dx.doi.org/10.1007/s11214-021-00841-8 , https://ui.adsabs.harvard.edu/abs/2021SSRv..217...65B 217, 65

Bardeen J. M., Press W. H., Teukolsky S. A., 1972, http://dx.doi.org/10.1086/151796 , https://ui.adsabs.harvard.edu/abs/1972ApJ...178..347B 178, 347

Begelman M. C., Blandford R. D., Rees M. J., 1984, http://dx.doi.org/10.1103/RevModPhys.56.255 Reviews of Modern Physics, https://ui.adsabs.harvard.edu/abs/1984RvMP...56..255B 56, 255

Berti E., Volonteri M., 2008, http://dx.doi.org/10.1086/590379 ApJ, 684, 822

Bicknell G. V., Begelman M. C., 1996, Astrophysical Journal v. 467, p. 597, 467, 597

Blandford R. D., Payne D. G., 1982, http://dx.doi.org/10.1093/mnras/199.4.883 , https://ui.adsabs.harvard.edu/abs/1982MNRAS.199..883B 199, 883

Blandford R. D., Znajek R. L., 1977, http://dx.doi.org/10.1093/mnras/179.3.433 , https://ui.adsabs.harvard.edu/abs/1977MNRAS.179..433B 179, 433

Bouman K. L., Johnson M. D., Zoran D., Fish V. L., Doeleman S. S., Freeman W. T., 2016, in Proceedings of the IEEE Conference on Computer Vision and Pattern Recognition (CVPR).

Brenneman L., 2013, Measuring the Angular Momentum of Supermassive Black Holes, http://dx.doi.org/10.1007/978-1-4614-7771-6. doi:10.1007/978-1-4614-7771-6.

Brenneman L. W., Reynolds C. S., 2006, http://dx.doi.org/10.1086/508146 , https://ui.adsabs.harvard.edu/abs/2006ApJ...652.1028B 652, 1028

Broderick A. E., Narayan R., Kormendy J., Perlman E. S., Rieke M. J., Doeleman S. S., 2015, http://dx.doi.org/10.1088/0004-637X/805/2/179 , https://ui.adsabs.harvard.edu/abs/2015ApJ...805..179B 805, 179

Bromberg O., Levinson A., 2009, http://dx.doi.org/10.1088/0004-637X/699/2/1274 , https://ui.adsabs.harvard.edu/abs/2009ApJ...699.1274B 699, 1274

Chael A., Issaoun S., Pesce D. W., Johnson M. D., Ricarte A., Fromm C. M., Mizuno Y., 2023, http://dx.doi.org/10.3847/1538-4357/acb7e4 , https://ui.adsabs.harvard.edu/abs/2023ApJ...945...40C 945, 40

Daly R. A., 2011, http://dx.doi.org/10.1111/j.1365-2966.2011.18452.x Monthly Notices of the Royal Astronomical Society, 414, 1253

Daly R. A., 2019, http://dx.doi.org/10.3847/1538-4357/ab35e6 , https://ui.adsabs.harvard.edu/abs/2019ApJ...886...37D 886, 37

Di Matteo T., Allen S. W., Fabian A. C., Wilson A. S., Young A. J., 2003a, in Collin S., Combes F., Shlosman I., eds, Astronomical Society of the Pacific Conference Series Vol. 290, Active Galactic Nuclei: From Central Engine to Host Galaxy. p. 391

Di Matteo T., Allen S. W., Fabian A. C., Wilson A. S., Young A. J., 2003b, http://dx.doi.org/10.1086/344504 , https://ui.adsabs.harvard.edu/abs/2003ApJ...582..133D 582, 133

Doeleman S. S., et al., 2012, http://dx.doi.org/10.1126/science.1224768 Science, https://ui.adsabs.harvard.edu/abs/2012Sci...338..355D 338, 355

Doeleman S. S., et al., 2023, http://dx.doi.org/10.3390/galaxies11050107 Galaxies, https://ui.adsabs.harvard.edu/abs/2023Galax..11..107D 11, 107

Dokuchaev V., Nazarova N., 2019, http://dx.doi.org/10.3390/universe5080183 Universe, 5, 183

EHTC et al., 2019a, http://dx.doi.org/10.3847/2041-8213/ab0ec7 , https://ui.adsabs.harvard.edu/abs/2019ApJ...875L...1E 875, L1

EHTC et al., 2019b, http://dx.doi.org/10.3847/2041-8213/ab0ec7 , https://ui.adsabs.harvard.edu/abs/2019ApJ...875L...1E 875, L1

EHTC et al., 2019c, http://dx.doi.org/10.3847/2041-8213/ab0c96 , https://ui.adsabs.harvard.edu/abs/2019ApJ...875L...2E 875, L2

EHTC et al., 2019d, http://dx.doi.org/10.3847/2041-8213/ab0e85 , https://ui.adsabs.harvard.edu/abs/2019ApJ...875L...4E 875, L4

EHTC et al., 2019e, http://dx.doi.org/10.3847/2041-8213/ab0f43 , https://ui.adsabs.harvard.edu/abs/2019ApJ...875L...5E 875, L5

EHTC et al., 2019f, http://dx.doi.org/10.3847/2041-8213/ab1141 , https://ui.adsabs.harvard.edu/abs/2019ApJ...875L...6E 875, L6

EHTC et al., 2021a, http://dx.doi.org/10.3847/2041-8213/abe71d , https://ui.adsabs.harvard.edu/abs/2021ApJ...910L..12E 910, L12

EHTC et al., 2021b, http://dx.doi.org/10.3847/2041-8213/abe4de , https://ui.adsabs.harvard.edu/abs/2021ApJ...910L..13E 910, L13

EHTC et al., 2022a, http://dx.doi.org/10.3847/2041-8213/ac6674 , https://ui.adsabs.harvard.edu/abs/2022ApJ...930L..12E 930, L12

EHTC et al., 2022b, http://dx.doi.org/10.3847/2041-8213/ac6672 , https://ui.adsabs.harvard.edu/abs/2022ApJ...930L..16E 930, L16

EHTC et al., 2024, http://dx.doi.org/10.1051/0004-6361/202347932 , https://ui.adsabs.harvard.edu/abs/2024AA...681A..79E 681, A79

Einstein A., 1915, Sitzungsberichte der Königlich Preussischen Akademie der Wissenschaften, https://ui.adsabs.harvard.edu/abs/1915SPAW.....844E pp 844–847

Fabian A. C., 2012, http://dx.doi.org/10.1146/annurev-astro-081811-125521 , https://ui.adsabs.harvard.edu/abs/2012ARAA..50..455F 50, 455

Feng J., Wu Q., 2017, http://dx.doi.org/10.1093/mnras/stx1283 , https://ui.adsabs.harvard.edu/abs/2017MNRAS.470..612F 470, 612

Foster J., Nightingale J. D., 2006, A Short Course in General Relativity, http://dx.doi.org/10.1007/978-0-387-27583-3. doi:10.1007/978-0-387-27583-3.

Frolov V. P., Zelnikov A., 2011, Introduction to black hole physics. Oxford Univ. Press, Oxford, http://dx.doi.org/10.1093/acprof:oso/9780199692293.001.0001 doi:10.1093/acprof:oso/9780199692293.001.0001, https://cds.cern.ch/record/1418196

Garofalo D., 2020, http://dx.doi.org/10.1002/andp.201900480 Annalen der Physik, https://ui.adsabs.harvard.edu/abs/2020AnP...53200480G 532, 1900480

Garofalo D., Evans D. A., Sambruna R. M., 2010, http://dx.doi.org/10.1111/j.1365-2966.2010.16797.x Monthly Notices of the Royal Astronomical Society, 406, 975

Gebhardt K., Adams J., Richstone D., Lauer T. R., Faber S. M., Gültekin K., Murphy J., Tremaine S., 2011, http://dx.doi.org/10.1088/0004-637X/729/2/119 , https://ui.adsabs.harvard.edu/abs/2011ApJ...729..119G 729, 119

Graham A. W., 2023, http://dx.doi.org/10.1093/mnras/stad1124 , https://ui.adsabs.harvard.edu/abs/2023MNRAS.522.3588G 522, 3588

Gürlebeck N., 2015, Physical review letters, 114 15, 151102

Hada K., et al., 2018, http://dx.doi.org/10.3847/1538-4357/aac49f , https://ui.adsabs.harvard.edu/abs/2018ApJ...860..141H 860, 141

Hawley J. F., Krolik J. H., 2006, http://dx.doi.org/10.1086/500385 , https://ui.adsabs.harvard.edu/abs/2006ApJ...641..103H 641, 103

Heckman T. M., Best P. N., 2014, Annual Review of Astronomy and Astrophysics, 52, 589

Hughes D. H., et al., 2010, in Stepp L. M., Gilmozzi R., Hall H. J., eds, Society of Photo-Optical Instrumentation Engineers (SPIE) Conference

Series Vol. 7733, Ground-based and Airborne Telescopes III. p. 773312, http://dx.doi.org/10.1117/12.857974 doi:10.1117/12.857974

Jeter B., Broderick A. E., McNamara B. R., 2019, http://dx.doi.org/10.3847/1538-4357/ab3221 , https://ui.adsabs.harvard.edu/abs/2019ApJ...882...82J 882, 82

Johannsen T., Psaltis D., 2010, http://dx.doi.org/10.1088/0004-637X/718/1/446 Astrophysical Journal, 718, 446

Johnson M. H., Teller E., 1982, http://dx.doi.org/10.1073/pnas.79.4.1340 Proceedings of the National Academy of Science, https://ui.adsabs.harvard.edu/abs/1982PNAS...79.1340J 79, 1340

Kawashima T., Kino M., Akiyama K., 2019, http://dx.doi.org/10.3847/1538-4357/ab19c0 The Astrophysical Journal, 878, 27

Kerr R. P., 1963, http://dx.doi.org/10.1103/PhysRevLett.11.237 , https://ui.adsabs.harvard.edu/abs/1963PhRvL..11..237K 11, 237

King A. R., Pringle J. E., Livio M., 2007, http://dx.doi.org/10.1111/j.1365-2966.2007.11556.x
, https://ui.adsabs.harvard.edu/abs/2007MNRAS.376.1740K 376, 1740

Kumar R., Ghosh S. G., 2020, http://dx.doi.org/10.1088/1475-7516/2020/07/053 , https://ui.adsabs.harvard.edu/abs/2020JCAP...07..053K 2020, 053

Kuo C. Y., et al., 2014, http://dx.doi.org/10.1088/2041-8205/783/2/L33 , https://ui.adsabs.harvard.edu/abs/2014ApJ...783L..33K 783, L33

Li L.-X., 2004, http://dx.doi.org/10.1093/pasj/56.4.685 , https://ui.adsabs.harvard.edu/abs/2004PASJ...56..685L 56, 685

Li Y.-R., Yuan Y.-F., Wang J.-M., Wang J.-C., Zhang S., 2009, http://dx.doi.org/10.1088/0004-637X/699/1/513 , https://ui.adsabs.harvard.edu/abs/2009ApJ...699..513L 699, 513

Lu R.-S., et al., 2023, http://dx.doi.org/10.1038/s41586-023-05843-w , https://ui.adsabs.harvard.edu/abs/2023Natur.616..686L 616, 686

Luminet J. P., 1979, , https://ui.adsabs.harvard.edu/abs/1979AA....75..228L 75, 228

Lynden-Bell D., 1969, http://dx.doi.org/10.1038/223690a0 , https://ui.adsabs.harvard.edu/abs/1969Natur.223..690L 223, 690

Mall G., Liu H., Bambi C., Steiner J. F., García J. A., 2024, http://dx.doi.org/10.1093/mnras/stad3933 , https://ui.adsabs.harvard.edu/abs/2024MNRAS.52712053M 527, 12053

Matveyenko L. I., Seleznev S. V., 2011, http://dx.doi.org/10.1134/S1063773711030030 Astronomy Letters, https://ui.adsabs.harvard.edu/abs/2011AstL...37..154M 37, 154

McKinney J. C., 2006, http://dx.doi.org/10.1111/j.1365-2966.2006.10256.x Monthly Notices of the Royal Astronomical Society, 368, 1561

McKinney J. C., Gammie C. F., 2004, The astrophysical journal, 611, 977

Medeiros L., Psaltis D., Özel F., 2020, http://dx.doi.org/10.3847/1538-4357/ab8bd1 , https://ui.adsabs.harvard.edu/abs/2020ApJ...896....7M 896, 7

Medeiros L., Psaltis D., Lauer T. R., Özel F., 2023, http://dx.doi.org/10.3847/2041-8213/acc32d , https://ui.adsabs.harvard.edu/abs/2023ApJ...947L...7M 947, L7

Meier D. L., 1999, http://dx.doi.org/10.1086/307671 , https://ui.adsabs.harvard.edu/abs/1999ApJ...522..753M 522, 753

Meier D. L., 2012, Black Hole Astrophysics: The Engine Paradigm, http://dx.doi.org/10.1007/978-3-642-01936-4. doi:10.1007/978-3-642-01936-4.

Meier D. L., Koide S., Uchida Y., 2001a, http://dx.doi.org/10.1126/science.291.5501.84 Science, https://ui.adsabs.harvard.edu/abs/2001Sci...291...84M 291, 84

Meier D. L., Koide S., Uchida Y., 2001b, Science, 291, 84

Mościbrodzka M., Dexter J., Davelaar J., Falcke H., 2017, http://dx.doi.org/10.1093/mnras/stx587 Monthly Notices of the Royal Astronomical Society, 468, 2214

Nakamura M., et al., 2018, http://dx.doi.org/10.3847/1538-4357/aaeb2d , https://ui.adsabs.harvard.edu/abs/2018ApJ...868..146N 868, 146

Narayan R., McClintock J. E., 2005, http://dx.doi.org/10.1086/428709 ApJ, 623, 1017

Narayan R., McClintock J. E., 2012, http://dx.doi.org/10.1111/j.1745-3933.2011.01181.x
, https://ui.adsabs.harvard.edu/abs/2012MNRAS.419L..69N 419, L69

Nemmen R., 2019a, http://dx.doi.org/10.3847/2041-8213/ab2fd3 ApJ, 880, L26

Nemmen R., 2019b, http://dx.doi.org/10.3847/2041-8213/ab2fd3 , https://ui.adsabs.harvard.edu/abs/2019ApJ...880L..26N 880, L26

Nokhrina E. E., Gurvits L. I., Beskin V. S., Nakamura M., Asada K., Hada K., 2019, http://dx.doi.org/10.1093/mnras/stz2116
, https://ui.adsabs.harvard.edu/abs/2019MNRAS.489.1197N 489, 1197

Owen F. N., Eilek J. A., Kassim N. E., 2000, http://dx.doi.org/10.1086/317151 , https://ui.adsabs.harvard.edu/abs/2000ApJ...543..611O 543, 611

Park J., et al., 2019, http://dx.doi.org/10.3847/1538-4357/ab5584 , https://ui.adsabs.harvard.edu/abs/2019ApJ...887..147P 887, 147

Pesce D. W., Palumbo D. C. M., Ricarte A., Broderick A. E., Johnson M. D., Nagar N. M., Natarajan P., Gómez J. L., 2022, http://dx.doi.org/10.3390/galaxies10060109 Galaxies, https://ui.adsabs.harvard.edu/abs/2022Galax..10..109P 10, 109

Prieto M. A., Fernández-Ontiveros J. A., Markoff S., Espada D., González-Martín O., 2016, http://dx.doi.org/10.1093/mnras/stw166 , https://ui.adsabs.harvard.edu/abs/2016MNRAS.457.3801P 457, 3801

Psaltis D., Özel F., Chan C.-K., Marrone D. P., 2015, http://dx.doi.org/10.1088/0004-637X/814/2/115 , https://ui.adsabs.harvard.edu/abs/2015ApJ...814..115P 814, 115

Psaltis D., et al., 2020, http://dx.doi.org/10.1103/PhysRevLett.125.141104 , https://ui.adsabs.harvard.edu/abs/2020PhRvL.125n1104P 125, 141104

Rafferty D. A., McNamara B. R., Nulsen P. E. J., Wise M. W., 2006, http://dx.doi.org/10.1086/507672 , https://ui.adsabs.harvard.edu/abs/2006ApJ...652..216R 652, 216

Raymond A. W., et al., 2024, http://dx.doi.org/10.3847/1538-3881/ad5bdb , https://ui.adsabs.harvard.edu/abs/2024AJ....168..130R 168, 130

Rees M. J., Begelman M. C., Blandford R. D., Phinney E. S., 1982, http://dx.doi.org/10.1038/295017a0 , https://ui.adsabs.harvard.edu/abs/1982Natur.295...17R 295, 17

Ressler S. M., White C. J., Quataert E., 2023, http://dx.doi.org/10.1093/mnras/stad837 , https://ui.adsabs.harvard.edu/abs/2023MNRAS.521.4277R 521, 4277

Reynolds C. S., 2013, http://dx.doi.org/10.1088/0264-9381/30/24/244004 Classical and Quantum Gravity, https://ui.adsabs.harvard.edu/abs/2013CQGra..30x4004R 30, 244004

Reynolds C. S., 2019a, Observing Black Holes Spin (http://arxiv.org/abs/1903.11704 arXiv:1903.11704)

Reynolds C. S., 2019b, http://dx.doi.org/10.1038/s41550-018-0665-z Nature Astronomy, https://ui.adsabs.harvard.edu/abs/2019NatAs...3...41R 3, 41

Reynolds C., 2021a, in 43rd COSPAR Scientific Assembly. Held 28 January - 4 February. p. 1412

Reynolds C. S., 2021b, http://dx.doi.org/10.1146/annurev-astro-112420-035022 , https://ui.adsabs.harvard.edu/abs/2021ARAA..59..117R 59, 117

Reynolds C. S., 2021c, http://dx.doi.org/10.1146/annurev-astro-112420-035022 Ann.Rev.A&A, 59, 117

Reynolds C. S., Fabian A. C., 2008, http://dx.doi.org/10.1086/527344 , https://ui.adsabs.harvard.edu/abs/2008ApJ...675.1048R 675, 1048

Reynolds C. S., Di Matteo T., Fabian A. C., Hwang U., Canizares C. R., 1996, http://dx.doi.org/10.1093/mnras/283.4.L111 , https://ui.adsabs.harvard.edu/abs/1996MNRAS.283L.111R 283, L111

Ricarte A., Tiede P., Emami R., Tamar A., Natarajan P., 2023, http://dx.doi.org/10.3390/galaxies11010006 Galaxies, https://ui.adsabs.harvard.edu/abs/2023Galax..11....6R 11, 6

Richstone D., et al., 1998, Supermassive Black Holes and the Evolution of Galaxies (http://arxiv.org/abs/astro-ph/9810378 arXiv:astro-ph/9810378)

Roelofs F., et al., 2023, http://dx.doi.org/10.3390/galaxies11010012 Galaxies, https://ui.adsabs.harvard.edu/abs/2023Galax..11...12R 11, 12

Royster M. J., Yusef-Zadeh F., Wardle M., Kunneriath D., Cotton W., Roberts D. A., 2019, http://dx.doi.org/10.3847/1538-4357/aafd38 , https://ui.adsabs.harvard.edu/abs/2019ApJ...872....2R 872, 2

Russell H. R., McNamara B. R., Edge A. C., Hogan M. T., Main R. A., Vantyghem A. N., 2013, http://dx.doi.org/10.1093/mnras/stt490 , https://ui.adsabs.harvard.edu/abs/2013MNRAS.432..530R 432, 530

Russell H. R., Fabian A. C., McNamara B. R., Broderick A. E., 2015, http://dx.doi.org/10.1093/mnras/stv954 , https://ui.adsabs.harvard.edu/abs/2015MNRAS.451..588R 451, 588

Shakura N. I., Sunyaev R. A., 1973, , https://ui.adsabs.harvard.edu/abs/1973AA....24..337S 24, 337

Sob'yanin D. N., 2018, http://dx.doi.org/10.1093/mnrasl/sly097 , https://ui.adsabs.harvard.edu/abs/2018MNRAS.479L..65S 479, L65

Stawarz Ł., Aharonian F., Kataoka J., Ostrowski M., Siemiginowska A., Sikora M., 2006, http://dx.doi.org/10.1111/j.1365-2966.2006.10525.x , https://ui.adsabs.harvard.edu/abs/2006MNRAS.370..981S 370, 981

Tamburini F., Thidé B., Della Valle M., 2020, http://dx.doi.org/10.1093/mnrasl/slz176 , https://ui.adsabs.harvard.edu/abs/2020MNRAS.492L..22T 492, L22

Tchekhovskoy A., Narayan R., McKinney J. C., 2011a, in American Astronomical Society Meeting Abstracts #218. p. 317.04

Tchekhovskoy A., Narayan R., McKinney J. C., 2011b, http://dx.doi.org/10.1111/j.1745-3933.2011.01147.x , https://ui.adsabs.harvard.edu/abs/2011MNRAS.418L..79T 418, L79

Thompson A. R., Moran J. M., Swenson George W. J., 2017, Interferometry and Synthesis in Radio Astronomy, 3rd Edition, http://dx.doi.org/10.1007/978-3-319-44431-4. doi:10.1007/978-3-319-44431-4.

Thorne K. S., 1974, http://dx.doi.org/10.1086/152991 , https://ui.adsabs.harvard.edu/abs/1974ApJ...191..507T 191, 507

Vasudevan R. V., Fabian A. C., Reynolds C. S., Aird J., Dauser T., Gallo L. C., 2016, http://dx.doi.org/10.1093/mnras/stw363 , https://ui.adsabs.harvard.edu/abs/2016MNRAS.458.2012V 458, 2012

Volonteri M., Madau P., Quataert E., Rees M. J., 2005, The Astrophysical Journal, 620, 69

Wald R., 2010, General Relativity. University of Chicago Press, https://books.google.ie/books?id=9S-hzg6-moYC

Walker R. C., Hardee P. E., Davies F. B., Ly C., Junor W., 2018, http://dx.doi.org/10.3847/1538-4357/aaafcc , https://ui.adsabs.harvard.edu/abs/2018ApJ...855..128W 855, 128

Walsh J. L., Barth A. J., Ho L. C., Sarzi M., 2013, http://dx.doi.org/10.1088/0004-637X/770/2/86 , https://ui.adsabs.harvard.edu/abs/2013ApJ...770...86W 770, 86

Wang J.-M., Li Y.-R., Wang J.-C., Zhang S., 2008, http://dx.doi.org/10.1086/587740 , https://ui.adsabs.harvard.edu/abs/2008ApJ...676L.109W 676, L109

Wang J.-M., Liu J.-R., Li Y.-R., Songsheng Y.-Y., Yuan Y.-F., Ho L. C., 2023, http://dx.doi.org/10.3847/2041-8213/ad0bd9 , https://ui.adsabs.harvard.edu/abs/2023ApJ...958L..40W 958, L40

Wielgus M., et al., 2020, http://dx.doi.org/10.3847/1538-4357/abac0d , https://ui.adsabs.harvard.edu/abs/2020ApJ...901...67W 901, 67

Wilson T. L., Rohlfs K., Hüttemeister S., 2013, Tools of Radio Astronomy, http://dx.doi.org/10.1007/978-3-642-39950-3. doi:10.1007/978-3-642-39950-3.

Young P. J., Westphal J. A., Kristian J., Wilson C. P., Landauer F. P., 1978, http://dx.doi.org/10.1086/156076 , https://ui.adsabs.harvard.edu/abs/1978ApJ...221..721Y 221, 721

Young A. J., Wilson A. S., Mundell C. G., 2002, http://dx.doi.org/10.1086/342918 , https://ui.adsabs.harvard.edu/abs/2002ApJ...579..560Y 579, 560